Journal of Magnetic Resonance 194 (2008) 264–282

Contents lists available at ScienceDirect

Journal of Magnetic Resonance

journal homepage: www.elsevier.com/locate/jmr

Practical aspects of Lee–Goldburg based CRAMPS techniques for high-resolution ^{1}H NMR spectroscopy in solids: Implementation and applications

Cristina Coelho [a], João Rocha [a], P.K. Madhu [b], Luís Mafra [a,*]

[a] Department of Chemistry, CICECO, University of Aveiro, 3810-193 Aveiro, Portugal
[b] Department of Chemical Sciences, Tata Institute of Fundamental Research, Homi Bhabha Road, Colaba, Mumbai 400 005, India

ARTICLE INFO

Article history:
Received 18 June 2008
Revised 15 July 2008
Available online 24 July 2008

Keywords:
^{1}H
Homonuclear techniques
2D homonuclear correlation
Solid-state NMR
Lee–Goldburg
High-resolution proton decoupling
LG decoupling
CRAMPS techniques
Inorganic–organic hybrids materials
FSLG
PMLG

ABSTRACT

Elucidating the local environment of the hydrogen atoms is an important problem in materials science. Because ^{1}H spectra in solid-state nuclear magnetic resonance (NMR) suffer from low resolution due to homogeneous broadening, even under magic-angle spinning (MAS), information of chemical interest may only be obtained using certain high-resolution ^{1}H MAS techniques. ^{1}H Lee–Goldburg (LG) CRAMPS (Combined Rotation And Multiple-Pulse Spectroscopy) methods are particularly well suited for studying inorganic–organic hybrid materials, rich in ^{1}H nuclei. However, setting up CRAMPS experiments is time-consuming and not entirely trivial, facts that have discouraged their widespread use by materials scientists. To change this *status quo*, here we describe and discuss some important aspects of the experimental implementation of CRAMPS techniques based on LG decoupling schemes, such as FSLG (Frequency Switched), and windowed and windowless PMLG (Phase Modulated). In particular, we discuss the influence on the quality of the ^{1}H NMR spectra of the different parameters at play, for example LG (Lee–Goldburg) pulses, radio-frequency (*rf*) phase, frequency switching, and pulse imperfections, using glycine and adamantane as model compounds. The efficiency and robustness of the different LG-decoupling schemes is then illustrated on the following materials: organo-phosphorus ligand, *N*-(phosphonomethyl)iminodiacetic acid [H_4pmida] [I], and inorganic–organic hybrid materials $(C_4H_{12}N_2)[Ge_2(pmida)_2OH_2]\cdot 4H_2O$ [II] and $(C_2H_5NH_3)[Ti(H_{1.5}PO_4)(PO_4)]_2\cdot H_2O$ [III].

1. Introduction

^{1}H is the most naturally abundant among the nuclear magnetic resonance (NMR) observable nuclear spins in organic molecules with high sensitivity, making it the most widely used nuclear probe in solution state NMR. ^{1}H chemical-shift ranges are well known and they are used to ascertain the presence of functional groups, yielding important information to chemists. In contrast, ^{1}H NMR is not routinely used to characterize solids, mainly because it is not straightforward to record high-resolution spectra, due to the strong ^{1}H–^{1}H homonuclear dipolar couplings, which broaden the spectral lines up to the kHz range. However, solid-state ^{1}H NMR is a powerful and unique local probe of the intermolecular interactions, such as strong and weak hydrogen-bonding [1–3] and π–π stacking effects [4], which determine the self-assembly of chemical species.

To remove the interactions which broaden the ^{1}H spectra resonances of solids, periodic multiple *rf* pulses and fast MAS (up to 70 kHz) have been used [5,6]. The latter consists in averaging out the space part of the ^{1}H homonuclear Hamiltonian by mechanical rotation of the sample, while the former entails the application of periodic multiple *rf* pulses, resulting in an averaging in the spin space. Considerable progress has been made in order to combine, in an efficient way, these two complementary approaches in CRAMPS schemes. Several strategies are available based on (i) windowless pulse schemes MREV-8 [7,8], WHH-4 [9], CORY-24 [10], BLEW-12 and -48 [11], MSHOT-3 [12], FSLG [13,14] or FFLG [15], PMLGn [16–18], DUMBO-1/eDUMBO [19–21], and (ii) windowed acquisition methods, BR-24 [22,23], wPMLGn [24,25], FSLG 240w [26], wDUMBO-1 [27]. CRAMPS experiments may also be classified according to the ratio between the *rf* multiple-pulse cycle time and the rotor period. Traditional CRAMPS uses long *rf* multiple-pulse periods and relatively slow spinning, while most recent CRAMPS techniques, such as FSLG, PMLG, and DUMBO employ much shorter *rf* cycle times, allowing higher spinning rates (up to 20 kHz). Other methods (not based on a quasi-static approximation) based on MAS synchronized sequences, using symmetry-based schemes, have been reported recently and demonstrated at 20–30 kHz MAS rate [28,29].

Lee–Goldburg based homonuclear decoupling schemes, are probably the most used pulse sequences for ^{1}H observation in

* Corresponding author.
E-mail address: lmafra@ua.pt (L. Mafra).

1090-7807/$ - see front matter © 2008 Elsevier Inc. All rights reserved.
doi:10.1016/j.jmr.2008.07.019

materials characterization. The simple LG decoupling has been also employed to aid in the measurement of ^{1}H-X dipolar couplings and to amplify the magnitude in the CSA of X nuclei [30,31]. FSLG and PMLG blocks have been successfully inserted during the t_1 evolution, in order to obtain a high-resolution ^{1}H spectra in the indirect dimension in 2D HOMCOR [16,32–34] and CP HETCOR [14,16,33–37]. LG-CP and FSLG-CP (or SEMA) based schemes may also be used to measure ^{1}H-X heteronuclear dipolar couplings and have been implemented in HOMCOR/HETCOR experiments to quench ^{1}H–^{1}H diffusion during cross-polarization or other evolution times, allowing to work in selective conditions [38–44]. In addition, Polarization Inversion and Spin Exchange at the Magic Angle (PISEMA) are experiments, consisting in a sensitivity enhancement method, which has shown to provide precise measurement of chemical shift and heteronuclear dipolar coupling interactions in strongly coupled ^{1}H–^{1}H systems [45]. The use of some of these techniques has been illustrated on small molecules [5,35,46–55] biological materials [27,56–68] photosynthetic pigments [69], inorganic materials [70], inorganic–organic hybrid materials [33,34,71–74] catalysts [75], nanoparticles [76], and pharmaceutical compounds [77].

Our aim for this work is both to provide a 'tutorial guide' for setting-up high-resolution ^{1}H LG-based NMR techniques using model compounds, and to illustrate the application of these methods to selected 'real' solids. The paper is, thus, divided in two parts. Firstly, the practical aspects concerning the full optimization of the LG-based CRAMPS, namely FSLG, PMLG, and wPMLG, sequences are presented and discussed step-by-step, using model compounds adamantane and glycine. Secondly, we exemplify the application of these techniques on selected organic molecules and inorganic–organic hybrid materials, stressing their ability to resolve crystallographically distinct ^{1}H resonances given by complex hydrogen-bonding networks, and to afford better resolution than moderately fast MAS (33 kHz). The performance of several LG-based decoupling methods will also be compared.

2. Principle of LG-based CRAMPS

2.1. FSLG (Frequency-Switched Lee–Goldburg) technique

Lee and Goldburg have shown that the application of an off-resonance *rf* field $\Delta\nu_{LG} = \frac{\nu_1}{\sqrt{2}}$ induces an effective field $\nu_{\text{eff}} = \sqrt{(\nu_1^2 + \Delta\nu^2)}$ inclined at the magic angle, $\theta_m = \arctan\left(\sqrt{2}\right) = \arctan\left(\frac{\nu_1}{\Delta\nu}\right)$, relative to the static magnetic field B_0. This effective field is parallel to a tilted rotating frame-z (toggling frame) axis, resulting in an efficient ^{1}H homonuclear decoupling. By applying periodic LG irradiation (perturbation) the spins precess around the effective field or magic-angle axis (1,1,1), thus canceling the dipolar Hamiltonian to first-order (it is zeroth-order in the language of Haeberlen which is anyway zero under MAS) over a period $\tau_{LG} = \sqrt{\frac{2}{3(\nu_1)^2}}$, the time to complete a 2π rotation in the toggling frame. By simultaneously switching the *rf* phase by 180° and the sign of the LG-offset frequency, the effective field direction may be inverted $(\nu_{\text{eff}} = \pm\frac{\Delta LG}{\cos\theta_m})$ producing a LG-type experiment symmetric by reflection, named Frequency-Switched Lee–Goldburg (FSLG). This experiment improves the dipolar truncation to second-order by eliminating all odd-order terms [8] to first-order, the homonuclear dipolar couplings are averaged out, whereas shielding (isotropic and anisotropic parts) is scaled by $\frac{1}{\sqrt{3}}$. In some consoles, this technique requires simultaneous switching of both the phase and frequency $\left(\Delta\nu_{LG} = \pm\frac{\nu_1}{\sqrt{2}}\right)$ at speeds <1 μs.

The FSLG method performs well for a spinning rate ν_R in the range of 10–16 kHz [35] with a further substantial improvement being possible if the sample volume is restricted by the application of a static magnetic field gradient and a selective pulse [78]. In modern NMR spectrometers the FSLG pulse sequence is relatively straightforward to implement, because the only adjustable parameters are the offset frequency $\Delta\nu_{LG}$ and the LG pulse length, the sequence is robust and may easily be fine tuned, if necessary.

2.2. PMLG (Phase-Modulated Lee–Goldburg) technique

Vega and co-workers [16] have presented a new class of CRAMPS experiments named Phase-Modulated Lee–Goldburg (PMLG). PMLG*n* is a phase-modulated version of FSLG, achieving line narrowing by the application of a series of discrete pulses nearly on resonance with appropriate phases. PMLG is composed of $2n$ pulses with the *rf* phase increment $\Delta\phi = \pm 207.8/n$ and starting with $\Delta\phi/2$ and $180 - (\Delta\phi/2)$, respectively. Although for a smooth *rf* profile the number of pulses in the PMLG units should be as large as possible, this will result in very short times for the pulse width which may result in undesirable phase glitches. In an ingenious reinterpretation of the LG concept, the zero-order or first order terms in the average Hamiltonian can be shown to vanish when the modulation of the pulse phase described by $\phi(t) = \omega_{PMLG}t$, satisfies the condition $|\omega_{PMLG}| = \omega_1/\sqrt{2}$ [16].

A full PMLG unit, for symmetrization arguments [79,80], takes either the form $x\bar{x}$ (PMLG$^+$) corresponding to a CRAMPS sequence starting with the *rf* field along the $+x$ direction and rotating counter clockwise, or the form $\bar{x}x$ (PMLG$^-$), corresponding to a CRAMPS sequence starting with *rf* along $-x$ and rotating clockwise (see Section 3.1 for a better understanding).

3. Experimental

^{1}H and ^{13}C spectra were recorded on a 9.4 T Bruker Avance 400 WB spectrometer (DSX model) on a 4 mm double-bearing probe at, respectively, 400.1 and 100.6 MHz. Samples were spun at the magic angle in 4 mm ZrO_2 rotors. In some cases, the sample was restricted to the center of the 4 mm rotor with the help of two (upper and lower) plastic inserts to improve the *rf* field homogeneity over the whole volume of the sample. However, no significant resolution enhancement was observed over the full-rotor acquisition. Quadrature detection in t_1 was achieved by the States-TPPI method. The correct ^{1}H chemical shifts and the scaling factor λ of ^{1}H CRAMPS (1D and 2D) spectra were determined by comparison with a ^{1}H CRAMPS spectra of glycine, which has well-resolved peaks allowing measurement of λ for a given *rf* field strength. Chemical shifts are quoted in parts per million (ppm) from tetramethylsilane (TMS).

The experimental parameters used for the different spectra are reported in the Tables below (Tables 1–6).

Table 1
Example of experimental parameters used to record the 1D ^{1}H–{CRAMPS}–^{13}C MAS NMR spectra of adamantane

	^{1}H{FSLG}–^{13}C	^{1}H{PMLG}–^{13}C
MAS rate (kHz)	12	12
Number of scans	8	4
Recycle delay (s)	3	3
^{1}H offset frequency (Hz)	−2000	2000
90°(^{1}H) pulse length (μs)	4	4.5
PMLG pulse unit (μs)	—	1.96
FSLG pulse unit (μs)	9.8	—
Frequency switching time (μs)	0.6	—
PMLG decoupling power (kHz)	—	86
FSLG decoupling power (kHz)	63	—
Positive LG offset frequency (+ΔLG) (Hz)	60925	—
Negative LG offset frequency (−ΔLG) (Hz)	−56925	—

Table 2
Experimental parameters used to record the 1D ^{1}H *w*PMLG spectra of glycine

	wPMLG5$^-$	*wPMLG5*$^+$	$\overline{wPMLG5^+}$	$\overline{wPMLG5^-}$
MAS rate (kHz)	12			
Number of scans	4			
Recycle delay (s)	1			
^{1}H offset frequency (Hz)	−5500	7000	7000	−5500
90°(^{1}H) pulse length (μs)	4.2			
PMLG pulse unit (μs)	1.7			
θ_m pulse length (μs)	1			
θ_m phase (degrees)	250			
Acquisition window t_w (μs)	6.4			
External dwell-pulse p_x (μs)	0.1			
90° (^{1}H) and θ_m power (kHz)	75			
PMLG decoupling power (kHz)	94			
BLKTR (μs)	0.2			
PHASPR (μs)	0.6	1	0.9	1

3.1. Pulse sequences

The basic schemes for ^{1}H homonuclear decoupling, are depicted in Fig. 1a and b for the FSLG and PMLG blocks, respectively. The FSLG block consists of two LG pulses separated by a delay t_s for frequency switching, between $+\Delta\nu_{LG}$ and $-\Delta\nu_{LG}$ offset frequencies, and 180° *rf* phase switching. The PMLG block is also composed of two LG units, each one divided into $n = 5$ discrete on-resonance pulses, with an *rf* phase (ϕ_i) increment. As FSLG, PMLG requires symmetrisation and, hence, the *rf* phases of the second LG pulse must be shifted 180° relative to the phases of the first LG unit. The evolution starts with 20.78° ($\Delta\phi_i/2$) and then each successive angle is determined by a 41.56° ($\Delta\phi_i = \pm 207.8/n$) increment. Hence for the PMLGn^+ (with $n = 5$) unit, $\phi_i = 20.78° + (i-1) \times 41.56°$, for pulses $i = 1$–5, and $\phi_i = 7.02° + (i-6) \times 41.56°$, for pulses $i = 6$–10. Similarly, for PMLG$^-$, $\phi_i = 159.22° + (i-1) \times 41.56°$, for pulses $i = 1$–5, and $\phi_i = 172.98° + (i-6) \times 41.56°$, for pulses $i = 6$–10. The ϕ_i values of *PMLG5*$^+$, *PMLG5*$^-$, $\overline{PMLG5^+}$ and $\overline{PMLG5^-}$ are, respectively (Fig. 1b), {20.78°, 62.34°, 103.90°, 145.56°, 187.02°, 7.02°, 325.46°, 283.39°, 242.34°, 200.78°}, {159.22°, 117.66°, 76.10°, 34.54°, 352.98°, 172.98°, 214.54°, 256.10°, 297.06°, 339.20°}, {200.78°, 242.34°, 283.39°, 325.46°, 7.02°, 187.02°, 145.46°, 103.90°, 62.34°, 20.78°} and {339.20°, 297.66°, 256.10°, 214.54°, 172.98°, 352.98°, 34.54°, 76.10°, 117.66°, 159.22°}.

The pulse sequences in Fig. 1c and d are used to perform a preliminary optimization of the scaling factor, *rf* field strength, and offset frequency for FSLG and PMLG blocks, via observation of the ^{13}C CH_2 and CH_3 *J*-multiplets. The pulse sequences depicted in Fig. 1e and f correspond to 2D ^{1}H{FSLG}–^{1}H and ^{1}H{PMLG*5*}–^{1}H

Table 3
Experimental parameters used to record the 2D ^{1}H{CRAMPS}–^{1}H and 2D ^{1}H{CRAMPS}–^{1}H{*w*PMLG} HOMCOR spectra of glycine

	^{1}H{FSLG}–^{1}H	^{1}H{PMLG}–^{1}H	^{1}H{FSLG}–^{1}H{*w*PMLG}	^{1}H{PMLG}–^{1}H{*w*PMLG}
MAS rate (kHz)	12	12.5	12	12
Number of scans	8	8	8	8
Number of t_1 points	170	256	300	512
Recycle delay (s)	0.8	0.8	0.8	0.8
^{1}H offset frequency (Hz)	−2000	−4800	−6000	−7000
90°(^{1}H) pulse length (μs)	3.2	3.35	4.2	4.2
PMLG pulse unit (μs)	–	1.75	–	2
*w*PMLG pulse unit (μs)	–	–	2	1.9
FSLG pulse unit (μs)	9.2	–	9.2	–
Frequency switching time (μs)	0.6	–	0.6	–
θ_m pulse length (μs)	1.5	2.04	2.55	1.4
Acquisition window t_w (μs)	–	–	6.3–7.0	6–6.4
External dwell-pulse p_x (μs)	–		0.1	0.1
Mixing time t_m (μs)	–	10	2–500	2–500
PMLG decoupling power (kHz)	–	84	84	84
FSLG decoupling power (kHz)	88	–	84	–
Positive LG offset frequency (+ΔLG) (Hz)	64,425	–	64,425	–
Negative LG offset frequency (−ΔLG) (Hz)	−53,425	–	−53,425	–

Table 4
Experimental parameters used to record the 2D ^{1}H{CRAMPS}–^{1}H and 2D ^{1}H{CRAMPS}–^{1}H{wPMLG} and 1D ^{1}H{*w*PMLG} spectra of **I**

	^{1}H{FSLG}–^{1}H	^{1}H{*w*PMLG}	^{1}H{PMLG}–^{1}H	^{1}H{FSLG}–^{1}H{*w*PMLG}
MAS rate (kHz)	14	14	14	14
Number of scans	8	32	8	8
Number of t_1 points	512	–	256	256
Recycle delay (s)	2	2	2	2
^{1}H offset frequency (Hz)	−2000	−6500	−7500	−6500
90°(^{1}H) pulse length (μs)	3.25	4.2	3.35	3.25
PMLG pulse unit (μs)	–	–	1.9	–
*w*PMLG pulse unit (μs)	–	1.7	–	2
FSLG pulse unit (μs)	9.2	–	–	9.2
Frequency switching time (μs)	0.6	–	–	0.6
θ_m pulse length (μs)	1.5	1.4	1.5	2
Acquisition window t_w (μs)	–	6.3	–	6.1
External dwell-pulse p_x (μs)	–	0.1	–	0.1
Mixing time t_m (μs)	–	–	10	–
PMLG decoupling power (kHz)	–	94	84	84
FSLG decoupling power (kHz)	85	–	–	84
Positive LG offset frequency (+ΔLG) (Hz)	65,925	–	–	64,425
Negative LG offset frequency (−ΔLG) (Hz)	−51,925	–	–	−53,425
BLKTR (μs)	–	0.2	–	–
PHASPR (μs)	–	0.6	–	–

Table 5
Experimental parameters used to record the 2D ^{1}H{CRAMPS}–^{1}H and 2D ^{1}H{CRAMPS}–^{1}H{*w*PMLG} HOMCOR and 1D ^{1}H *w*PMLG spectra of **II**

	^{1}H MAS	^{1}H{*w*PMLG}	^{1}H{FSLG}–^{1}H	^{1}H{FSLG}–^{1}H{*w*PMLG}	^{1}H{PMLG}–^{1}H
MAS rate (kHz)	30	12.5–14	14	14	14
Number of scans	8	32	8	16	8
Number of t_1 points	–	–	196	200	256
Recycle delay (s)	3	3	3	5	3
^{1}H offset frequency (Hz)	−5600	−6500	−2000	−6500	−7500
90°(^{1}H) pulse length (μs)	3.5	4.2	4.2	4.2	3.35
PMLG pulse unit (μs)	–	–	–	–	1.9
*w*PMLG pulse unit (μs)	–	1.7	–	2	–
FSLG pulse unit (μs)	–	–	9.2	9.2	–
Frequency switching time (μs)	–	–	0.6	0.6	–
θ_m pulse length (μs)	–	1	1.5	2.25	1.5
Acquisition window t_w (μs)	–	6.3	–	6.1	–
External dwell-pulse p_x (μs)	–	0.1	–	0.1	–
Mixing time t_m (μs)	–	–	2	2	2
PMLG decoupling power (kHz)	–	84	–	84	84
FSLG decoupling power (kHz)	–	–	85	84	–
Positive LG offset frequency (+ΔLG) (Hz)	–	–	64,425	64,425	–
Negative LG offset frequency (−ΔLG) (Hz)	–	–	−53,425	−53,425	–
BLKTR (μs)	–	0.4	–	–	0.2
PHASPR (μs)	–	0.6	–	–	0.6

Table 6
Experimental parameters used to record the 2D ^{1}H{CRAMPS}–^{1}H{*w*PMLG} HOMCOR spectra of **III**

	^{1}H{FSLG}–^{1}H{*w*PMLG}	^{1}H{PMLG}–^{1}H{*w*PMLG}
MAS rate (kHz)	12.5	12.5
Number of scans	16	8
Number of t_1 points	512	512
Recycle delay (s)	1	4
^{1}H offset frequency (Hz)	−6500	−7000
90°(^{1}H) pulse length (μs)	4.2	4.2
PMLG pulse unit (μs)	–	2
*w*PMLG pulse unit (μs)	2	1.9
FSLG pulse unit (μs)	9.2	–
Frequency switching time (μs)	0.6	–
θ_m pulse length (μs)	2.55	1.4
Acquisition window t_w (μs)	6.1–6.3	6
External dwell-pulse p_x (μs)	0.1	0.1
Mixing time t_m (μs)	2–500	2
90°(^{1}H) and θ_m power (kHz)	75	75
PMLG decoupling power (kHz)	84	84
FSLG decoupling power (kHz)	84	–
Positive LG offset frequency (+ΔLG) (Hz)	64,425	–
Negative LG offset frequency (−ΔLG) (Hz)	53,425	–

HOMCOR experiments, where Fig. 1a and b building blocks, respectively, may be inserted during t_1 evolution. In our spectrometer best results are obtained when the pulse sequences start with a $\pi/2 + \theta_m$ pulse that creates magnetization in the plane perpendicular to the direction of the effective *rf* field, the tilted *z*-axis [14]. Then, CRAMPS homonuclear decoupling is introduced and, at the end of the t_1 evolution, a $\pi/2 - \theta_m$ (=θ_c) pulse places the magnetization along the rotating-frame *z*-axis. The last $\pi/2$ pulse brings the magnetization back to the *xy* transverse plane for detection. ^{1}H spin diffusion may be studied by adding a mixing time t_m just before the last $\pi/2$ pulse. It is worth mentioning that other authors may perform these experiments in a slightly different way. For example, the pulse sequence may be initiated by a single $\pi/2$ pulse [81]; however the addition of a pre-pulse θ_m pulse may help optimizing the ^{1}H spectra in the t_1 dimension. The influence of θ_m will be discussed later.

Fig. 1g shows the pulse sequence used to record high-resolution 1D ^{1}H NMR spectra, with windowed acquisition of the sampled data points during signal detection (t_2), i.e., the data sampling is interrupted periodically (t_2 windows, t_W) for insertion of PMLG blocks.

The pulse schemes (Fig. 1h and i) used in 2D ^{1}H{FSLG}–^{1}H{*w*PMLG} and 2D ^{1}H{PMLG}–^{1}H{*w*PMLG} afford ^{1}H–^{1}H spectra exhibiting high resolution t_1 and t_2 dimensions using, respectively, windowless and windowed ^{1}H–^{1}H decoupling. In such experiments, the t_1 and t_2 homonuclear decouplings are optimized separately. The windowless decoupling (t_1) may be optimized using 1D (Fig. 1c and d) or 2D (Fig. 1e and f) pulse sequences. The windowed PMLG decoupling (t_2) is optimized by employing the 1D ^{1}H *w*PMLG sequence (Fig. 1g). The different optimizations steps are now discussed.

4. Results and discussion

The optimization of, among others, the following parameters in LG-based CRAMPS sequences will be discussed using model compounds adamantane and glycine: LG *rf* field strength, ^{1}H *rf* offset, rotation frequency, and variation of the scaling factor.

Among the different PMLG*n* sequences, those with $n = 3$, 5 and 9 are the most commonly used. Here, we deal mainly with the PMLG5 scheme because of its wide application at moderately high spinning frequencies [17].

4.1. Optimizing FSLG and PMLG ^{1}H–^{1}H decoupling via 1D spectra

1D ^{1}H–^{13}C experiments (Fig. 1a,b) are very useful to optimize the FSLG and PMLG unit blocks, and they consist in monitoring the ^{13}C J_{CH} splitting values of CH_2 and CH_3 while changing the pulse sequence parameters (^{1}H *rf* field strength, and *rf* offset). The shape and resolution of the ^{13}C *J*-multiplets are very sensitive to the misset of the parameters. For instance, through the direct observation of the experimentally scaled *J*-coupling and comparison with the solution NMR *J*-coupling values [82] the experimental scaling factors may be estimated.

4.1.1. LG rf field strength and ^{1}H rf offset

These are the two critical parameters to be optimized in FSLG and PMLG decoupling schemes. LG *rf* field strength is the power level to be applied during each LG unit. Keeping the *rf* offsets ($\pm\Delta\nu_{LG}$) and LG pulse (τ_{LG}) length (see experimental section) fixed to their theoretical values, one may easily tune the LG *rf* field strength until a good-quality spectrum is obtained. Fig. 2a and b gives a plot of

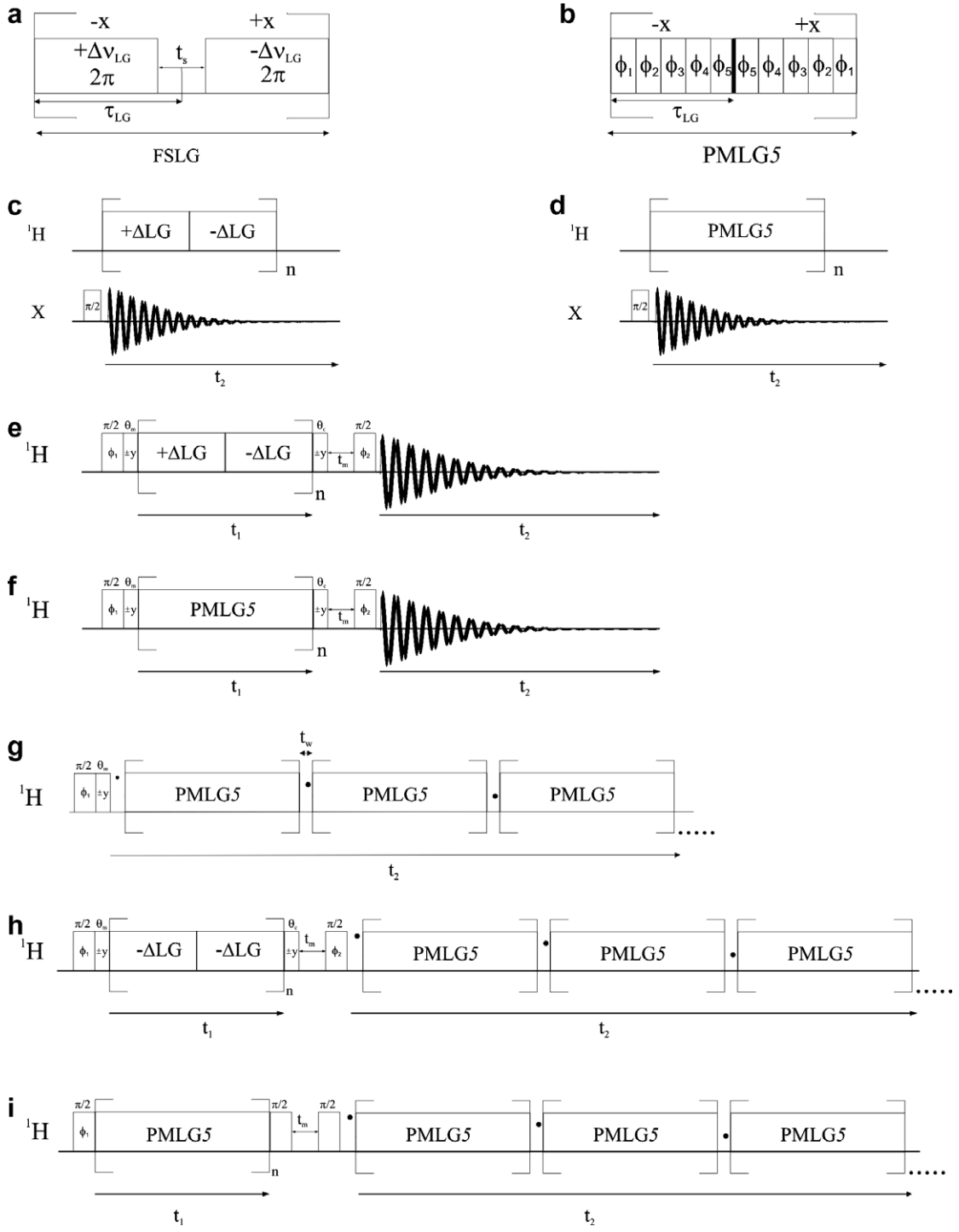

Fig. 1. (a) FSLG and (b) PMLG5 decoupling blocks. Pulse sequences used for ^{13}C observation employing (c) ^{1}H{FSLG} and (d) ^{1}H{PMLG} dipolar decoupling during t_2. Pulse sequences used for (e) 2D ^{1}H{FSLG}–^{1}H HOMCOR, (f) 2D ^{1}H{PMLG}–^{1}H HOMCOR, (g) 1D *w*PMLG5; (h) 2D ^{1}H{FSLG}–^{1}H{*w*PMLG5} HOMCOR and (i) 2D ^{1}H{PMLG5}–^{1}H{*w*PMLG5} HOMCOR ^{1}H MAS NMR experiments. Phase cycling: (e) $\phi_1 = +y, -y$; $\phi_2 = +x, +x, -x, -x, +y, +y, -y, -y$; $\phi_{rec} = +x, -x, -x, +x, +y, -y, -y, +y$; (f) $\phi_1 = +x, -x$; $\phi_2 = +x, +x, -x, -x, +y, +y, -y, -y$; $\phi_{rec} = +x, -x, -x, +x, +y, -y, -y, +y$; (g) $\phi_1 = +x, +y, -x, -y$; $\phi_{rec} = +x, +y, -x, -y$; (h) $\phi_1 = +y, -y$; $\phi_2 = +x, +x, -x, -x, +y, +y, -y, -y$; $\phi_{rec} = +x, -x, -x, +x, +y, -y, -y, +y$; (i) $\phi_1 = +x, +y, -x, -y$; $\phi_2 = +y, -x, -y, +x$; $\phi_{rec} = +x, +y, -x, -y$.

the experimental scaling factors against the *rf* field strength for FSLG and PMLG, respectively. Except at lower *rf* field strengths, where FSLG performs better than PMLG, the curves are similar. The best spectra (spectra 1 and 2, respectively, in Fig. 2a and b) are obtained for scaling factor of ca. 0.6, close to the theoretical $1/\sqrt{3}$ value. With all the other parameters unchanged, it is observed that additional power must be delivered in PMLG ($\nu_1 = 85.7$ kHz), in comparison with FSLG decoupling ($\nu_1 = 62.8$ kHz) in order to obtain the best-resolved spectra. However, comparing both spectra (Fig. 2a and b) the best resolved spectrum is obtained using the PMLG block, which shows the better resolution enhancement of PMLG compared to the FSLG scheme.

The ^{1}H *rf* offset affects both the spectral resolution and the scaling factor. The influence of the ^{1}H *rf* offset on the scaling factor, which is translated into spectral resolution, is depicted in Fig. 3a for FSLG, showing that at the exact LG offset condition,

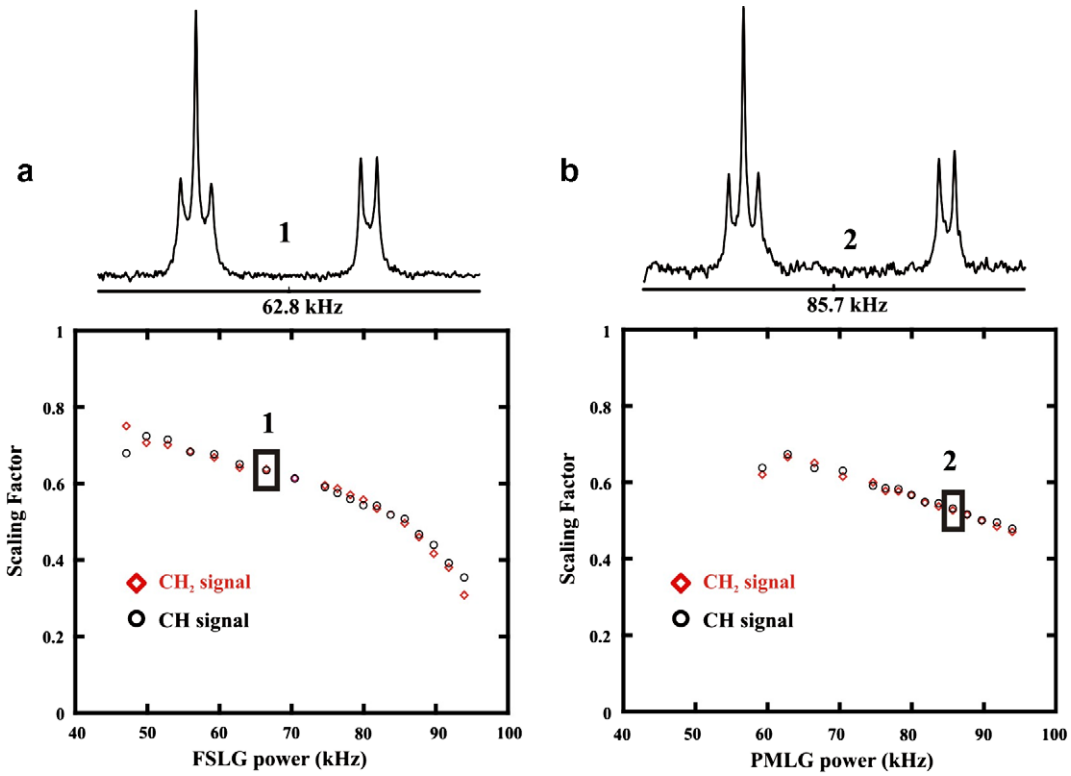

Fig. 2. Plot showing the scaling factor variation with the change of (a) FSLG and (b) PMLG5 ^{1}H *rf* decoupling strengths by monitoring the *J*-multiplets of adamantane –CH(○) and –CH_2 (◇) ^{13}C resonances, using pulse sequences of Fig. 1c and d, respectively.

$\Delta\nu_{LG} = \pm\frac{\nu_1}{\sqrt{2}}$ (i.e. without applying any asymmetric offset), the scaling factor tends to 0 degrading the spectral resolution (spectrum 1 in Fig. 3a). Increasing the asymmetric offset (ν_{lg}) gives rise to better spectra and a roughly constant scaling factor is obtained between ν_{lg} = ±5 to ν_{lg} = ±10 kHz. Employing symmetric LG ^{1}H offsets does not lead to a constant scaling factor region (Fig. 3b). Thus, the addition of correct asymmetric offsets to the FSLG offset condition ($\Delta\nu_{LG} = \pm\frac{\nu_1}{\sqrt{2}} \pm \nu_{lg}$) is essential to obtain optimum results.

The influence of the ^{1}H *rf* offset on the PMLG scaling factor values (Fig. 3c) is quite similar to that of FSLG (Fig. 3a), also showing a constant scaling factor region between ^{1}H *rf* offset values of ±5 and ±10 kHz.

4.1.2. Frequency switching time (t_s) in FSLG experiments

To guarantee a correct inversion of the *rf* phase between consecutive LG pulses, an intermediate switching delay was introduced between them (Fig. 1a) and optimized by observation of the *J*-coupling multiplets of adamantane. The optimization of this parameter (t_s) is mandatory, at least in old spectrometer consoles, to obtain highly resolved ^{1}H spectra. If t_s is too short or too long, the resolution degrades rapidly (Fig. 4).

4.1.3. Influence of the rotation frequency (ν_R) in FSLG experiments

Applying a standard *rf* field strength of 83 kHz for LG pulses, the resolution of the ^{13}C *J*-muliplets deteriorates above 12 kHz (spectra 1 and 2 Fig. 5). This effect is expected because the FSLG performance depends on the ratio between the FSLG cycle and rotor period, thus changing the *rf* field strength implies also changing the MAS rate to achieve optimal results. The same effect is observed in PMLG. Fig. 5 shows that although the spinning rate is altered the scaling factor does not change significantly. Contrarily, the spectral resolution may change at different MAS rates. It is, thus, important to carefully choose a suitable rotation frequency for a given ^{1}H *rf* field strength.

4.2. Optimizing FSLG and PMLG ^{1}H–^{1}H decoupling via 2D homonuclear correlation spectra

4.2.1. LG rf field strength and the PMLG unit pulse

Although the optimization of the *rf* field strength for FSLG and PMLG, respectively, have been carried out by acquiring multiple adamantane 1D spectra through ^{13}C observation, the power level derived from these experiments rarely corresponds to the best results obtained in a 2D experiment. Therefore, for optimum results, the ^{1}H CRAMPS decoupling efficiency must be checked in the indirect dimension of 2D ^{1}H {CRAMPS}–^{1}H HOMCOR experiments on glycine. The influence of the *rf* field strength on 2D FSLG and PMLG-based spectra is shown in Figs. 6a–e and 7a–e, respectively. For example, Fig. 7c and d, shows how the ^{1}H resolution is modified by changing the PMLG *rf* field by 0.2 db (~2 kHz). We also tested how sensitive the ^{1}H spectra are to the changes in the PMLG pulse unit (Fig. 8a–e). Best results are obtained using a pulse length of 1.75 μs and $\nu_1^{PMLG} = 84$ kHz (Fig. 8c). Altogether, Figs. 7 and 8 show that even slight changes in the setup parameters may considerably affect the PMLG sequences.

4.2.2. The axial F1 artifact

In general, all 2D ^{1}H{CRAMPS}–^{1}H spectra display an artifact in the center of the F1 dimension when FSLG and PMLG decoupling is occurring during the t_1 evolution. The axial artifact introduces undesirable wiggles in the spectra, which may compromise seriously the quality of the high-resolution ^{1}H spectrum. For FSLG, we show that by optimizing the *rf* field strength and the θ_m pulse length it is possible to overcome this problem. The F1 artifact appears when the ^{1}H magnetization is not perfectly perpendicular to the effective field direction, arising from the creation of zero-order coherence during the FSLG spin-lock pulses. It worsens as the *rf* field strength increases (Figs. 9 and 10) and therefore it must be minimized. Our experience indicates that best results, in terms of

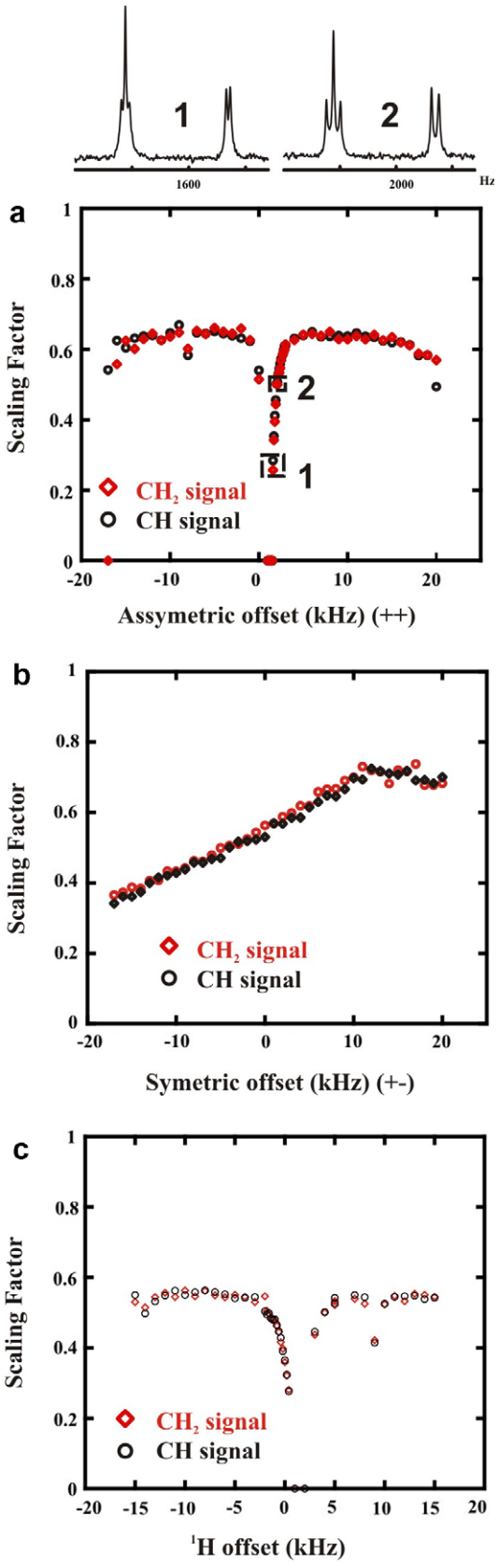

Fig. 3. Dependence of scaling factor on the ^{1}H offset irradiation frequency of (a–b) FSLG (using ^{1}H *rf* (a) asymmetric and (b) symmetric offsets) and PMLG5 decoupling, by monitoring the *J*-multiplets of adamantane –CH(○) and –CH_2 (◇) ^{13}C resonances using pulse sequences of Fig. 1c and d, respectively.

resolution, are obtained when the artifacts remain in the spectra, with intermediate intensity. Although the minimization of the artifact may be accomplished by reducing the FSLG *rf* field strength, a simultaneous decrease in spectral resolution is observed (Fig. 6a–e), hence, a compromise must be found between lowering the *rf* field strength and minimizing the F1 artifact. Other approaches to optimize the F1 artifact intensity and quadrature detection errors consist in tuning the lengths and phases of the *rf* pulses immediately preceding and following the FSLG block. For example, the artifact may be significantly reduced after optimizing the θ_m pulse length: when $\theta_m = 1.5$ μs the artifact is almost completely suppressed (Figs. 9d and 10b).

Although the CRAMPS ^{1}H *rf* field strength and θ_m *rf* pulse adjustment may, in some cases, lead to the complete absence of the F1 artifact, it may be difficult to achieve such condition in an affordable optimization time. This central artifact is, in general, always present and thus the sample resonances must be moved out of the center of F1 window. This means using a 2- or 3-fold F1 sweeping width, leading to longer acquisition times, if one wants to avoid such artifact.

4.3. Optimizing the windowed PMLG experiment

Windowed acquisition of ^{1}H NMR spectra affords highly resolved ^{1}H spectra in a single dimension, by direct stroboscopic observation of the ^{1}H signal. The ease of implementation of such strategy is highly depend on the hardware specifications of the spectrometer. In our old Bruker DSX console such experiments were not trivial because several spectrometer time constants had to be changed manually in order to record good quality spectra. Even a very small mis-set of such default spectrometer constants resulted in a total degradation of the ^{1}H spectral resolution. One of the main advantages of windowed acquisition schemes is the possibility to calibrate all the parameters by the direct observation of their influence on the ^{1}H spectra in only a few scans. We now discuss the influence of several experimental parameters on the quality of 1D ^{1}H *w*PMLG5 spectra.

4.3.1. Spectrometer constants

Although in more recent spectrometers such parameters are not under the user's control we think it is useful to show their effect in ^{1}H spectra, especially for those researchers who are still using older consoles. The relevant spectrometer default timings, for the optimization of the *w*PMLG experiment are the transmitter blanking time (*BLKTR*) and the phase presetting (*PHASPR*) [83]. The former consists in adding a blanking time just before the beginning of the *rf* pulse and its optimization is still critically necessary in last generation consoles. The principle of blanking is used in the Amplitude Setting Unit (ASU) and transmitter. The ASU and transmitter are blanked *BLKTR* μs before the pulse, i.e., their inputs are closed to incoming signals, during intervals of *BLKTR* μs immediately following detection of each transmitted *rf* pulse, protecting the receiver from noise during the intervals between incoming pulses. The latter is related with the time needed for the phase switching involved in a pulse program, where often several changes on the *rf* pulse phases take place. Then, a *PHASPR* μs time is needed to insure a stable phase when the pulse begins. Fig. 11a and b shows the evolution of the spectra as *BLKTR* and *PHASPR* are changed. On glycine, best results are obtained when *BLKTR* = 0.2 μs and *PHASPR* = 0.6 μs.

4.3.2. PMLG pulse length, external dwell pulses and acquisition window

In *w*PMLG experiments the basic unit consists of PMLG block and the acquisition window, thus the cycle time is $t_C = t_{PMLG} + t_W$ (Fig. 1g). The addition of t_W will decrease the characteristic fre-

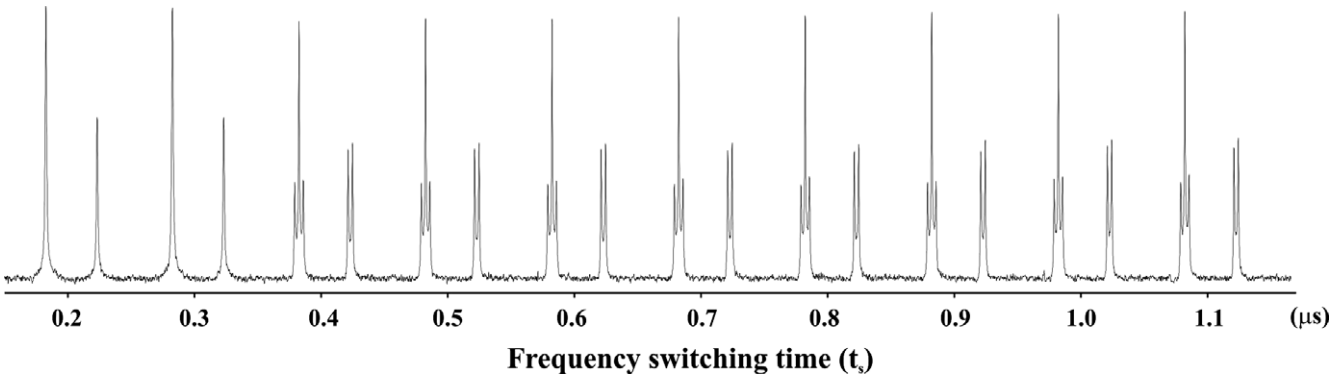

Fig. 4. Optimization of the FSLG frequency switching time t_s (μs) using pulse sequence of Fig. 1c.

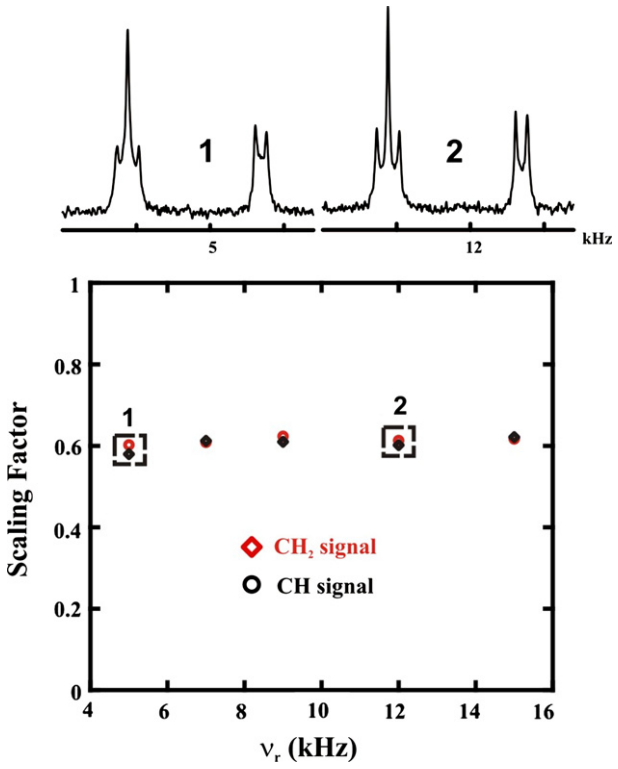

Fig. 5. Influence of the rotation frequency on the ^{13}C spectra of adamantane, using FSLG decoupling (ν_1 = 84 kHz).

quency, ν_C, of the *w*PMLG sequence with respect to the windowless PMLG sequence (Fig. 11e), which may need further optimization to avoid interference between MAS and spin space modulations. t_W is composed of the external dwell-pulse, p_x used to acquire a complex data point plus a given delay, t_x, necessary before the upcoming PMLG block. The sum of both refers to the acquisition window (t_W). To optimize the *w*PMLG5 window part, t_W and p_x must be tuned (Fig. 11c and d, respectively). Increasing p_x above a certain limit yields more artifacts, although it does not affect the spectral resolution. A p_x value as short as possible (0.1 μs in our case) is recommended. In the case of t_W, an increase generally leads to cleaner spectra, although the resolution is sacrificed. Optimum results have been obtained at t_W = 6.3 μs. but above and below this value the quality of the spectrum degrades quickly (Fig. 11c). During optimization we have noticed that the spectrum improves and worsens in a more or less random way for a given t_W. Indeed, a slightly mistuned wobble curve may drastically affect spectral quality and therefore a higher value of t_W is necessary to compensate it. The effect of the spectrometer mistuning on ^1H spectra is shown in Figure S1a–h.

4.3.3. Spinning rate

The spinning rate must be chosen in order to obtain the best results and to avoid obvious degeneracies where $k\nu_C = n\nu_R$ values (ν_C—characteristic frequency of the CRAMPS cycle; ν_R—rotation frequency) with k and n = ±1, ±2, ±3, ±4 [17,25]. Destructive interferences between MAS and homonuclear decoupling due to the crossing conditions typically happen when the integer ratio between the rotor period and the decoupling cycle time is $\tau_R/\tau_C < 5$, leading to line broadening. Efficient decoupling is only obtained if $\tau_R/\tau_C > 3$ but avoiding the resonance condition $\tau_R/\tau_C = 4$ [84]. For example at ν_R = 14.3 kHz (Fig. 11h), the resolution is worse because it is close to the condition ν_C (42.9 kHz) = **3**ν_R. Best results are obtained for a moderately high spinning rate (12–15 kHz) avoiding interference between MAS and spin modulations [85].

4.3.4. Axial artifact

Alike 2D schemes, a θ_m *rf* pulse may also be inserted just after the initial π/2 pulse to minimize the axial artifact. Adjusting the θ_m *rf* pulse length and phase affords a spectrum free from the central artifact. The effect of this optimization is shown in Fig. 11f and g. However, the application of an effective *z*-rotation [24] during the homonuclear decoupling sequences present cleaner ^1H spectra free from zero frequency artifacts thus avoiding the need for using such θ_m *rf* pulses.

4.3.5. Scaling factor

Fig. 12 shows the dependence of the effective off-resonance value ΔN (i.e., the difference between the irradiation offset frequency and the on-resonance frequency selected by the user) on the measured chemical shift values (i.e., the difference between the offset frequency corresponding to the peak position on ^1H CRAMPS spectra and the on-resonance frequency of this peak) for the different offsets used, $\Delta\nu$ on the different *w*PMLG phase variants. Measuring ΔN as a function of $\Delta\nu$ permits assessing the scaling factor $s = \Delta N/\Delta\nu$, ca. 0.69–0.70 in our spectrometer, which is different from other reported values [24,25]. Either for $\Delta N > 0$ or $\Delta N < 0$ the ΔN value has a linear relationship with respect to $\Delta\nu$.

4.3.6. Comparison of the different wPMLG variants

Fig. 13a–d shows the ^1H high-resolution spectrum of glycine obtained with *wPMLG5*$^-$, *wPMLG5*$^+$, *w*$\overline{PMLG5}^+$ and *w*$\overline{PMLG5}^-$, respectively. The spectral resolution of the CH_2 peaks using *wPMLG 5*$^+$ for $\Delta\nu = -7300$ Hz is slightly lower that the resolution obtained with *wPMLG5*$^-$ for $\Delta\nu$ = +4110 Hz. The peaks closer to the carrier frequency exhibit better resolution, as shown by Vega et al. [25], which explains the difference in the CH_2 resolution. No differences

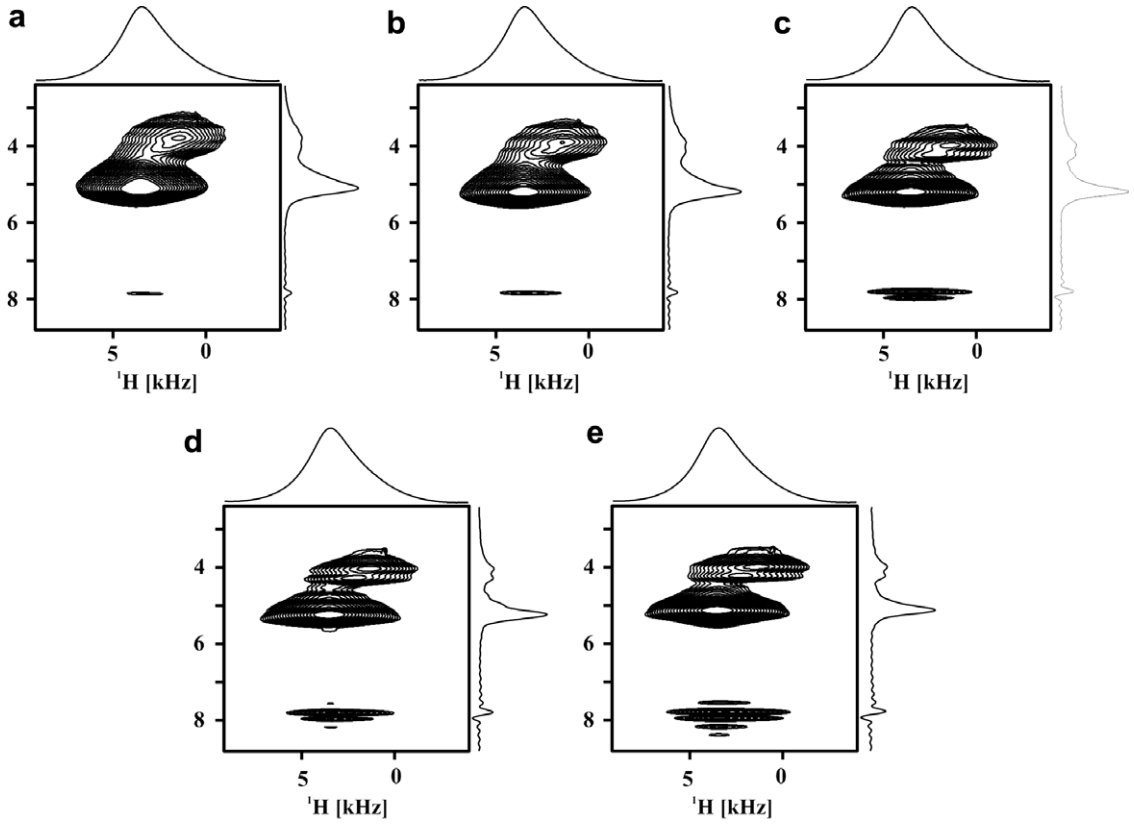

Fig. 6. 2D ^{1}H{FSLG}–^{1}H HOMCOR spectra of glycine recorded with different *rf* field strengths for FSLG decoupling employed during the t_1 dimension (Fig. 1e). The FSLG *rf* field strengths used were: (a) 70 kHz, (b) 75 kHz, (c) 82 kHz, (d) 84 kHz and (e) 88 kHz.

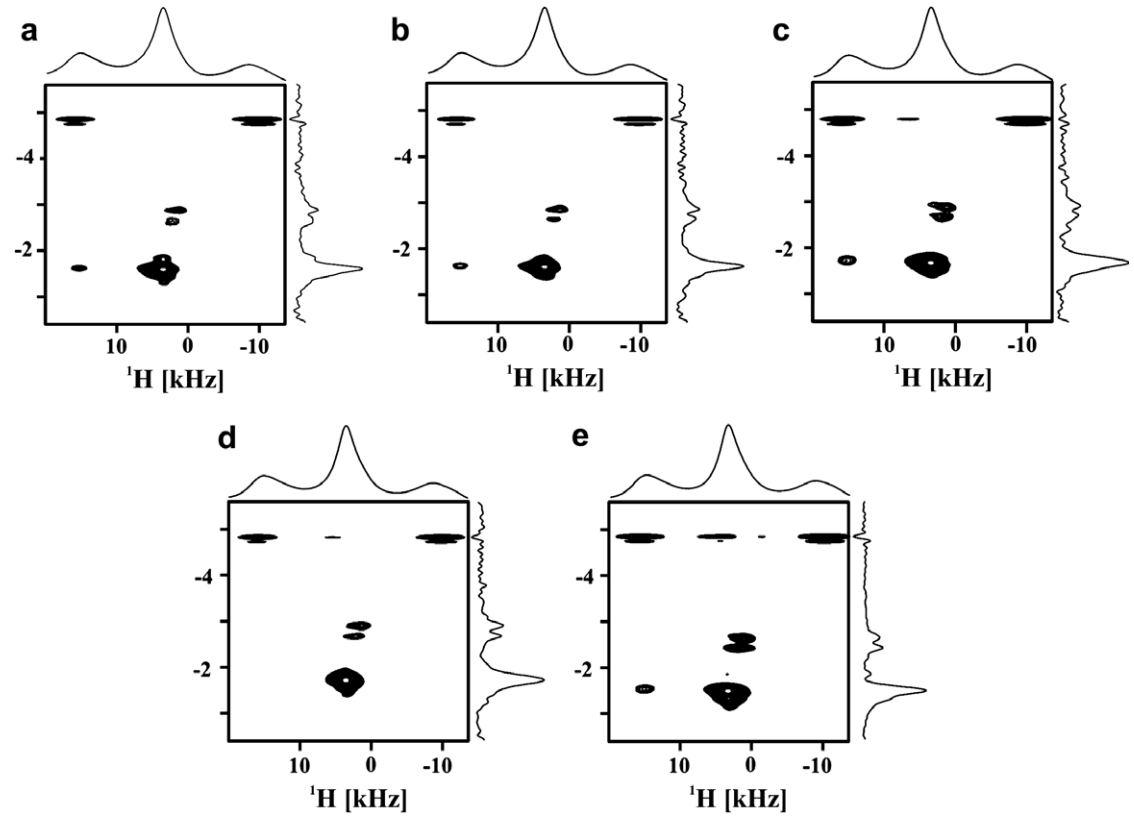

Fig. 7. 2D ^{1}H{PMLG}–^{1}H HOMCOR spectra of glycine recorded with different *rf* field strengths for PMLG5 decoupling employed during the t_1 dimension (Fig. 1f). The PMLG5 *rf* field strengths used were: (a) 71 kHz, (b) 75 kHz, (c) 82 kHz, (d) 84 kHz and (e) 88 kHz.

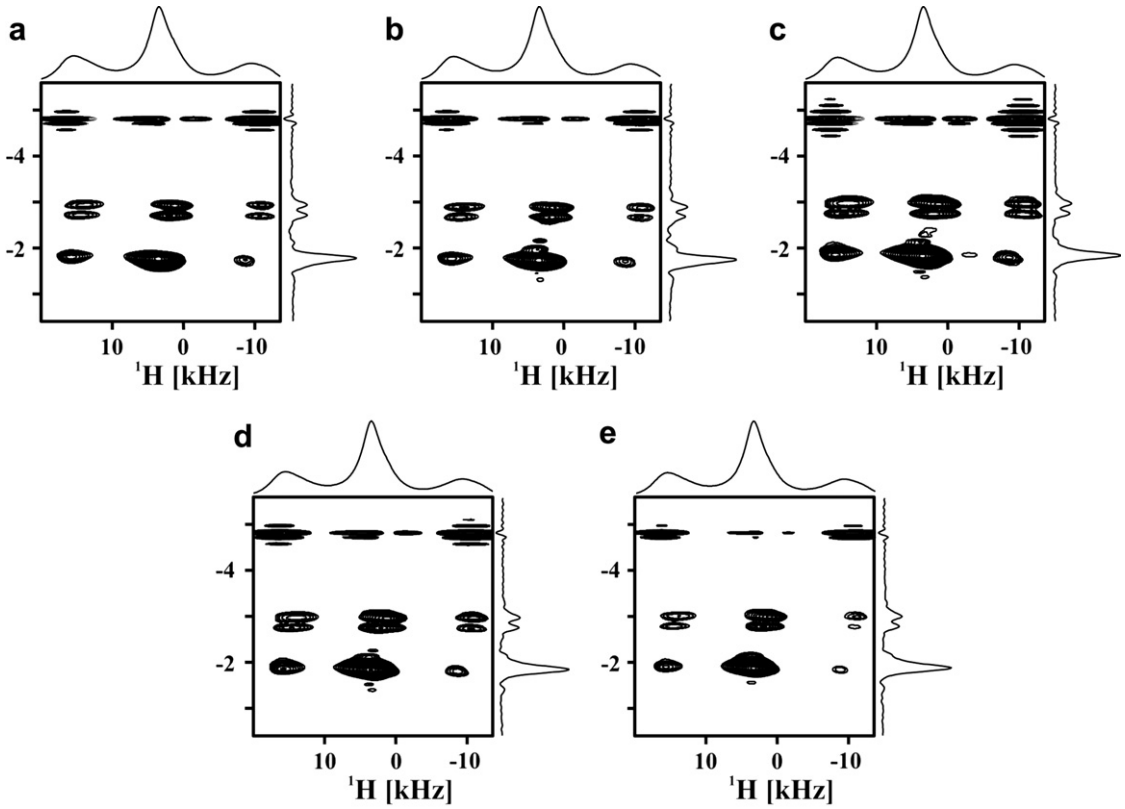

Fig. 8. 2D ^{1}H{PMLG}–^{1}H HOMCOR spectra of glycine recorded with different PMLG unit pulse lengths (Fig. 1f). The PMLG unit pulses used are: (a) 1.9 μs, (b) 1.8 μs, (c) 1.75 μs, (d) 1.7 μs and (e) 1.65 μs.

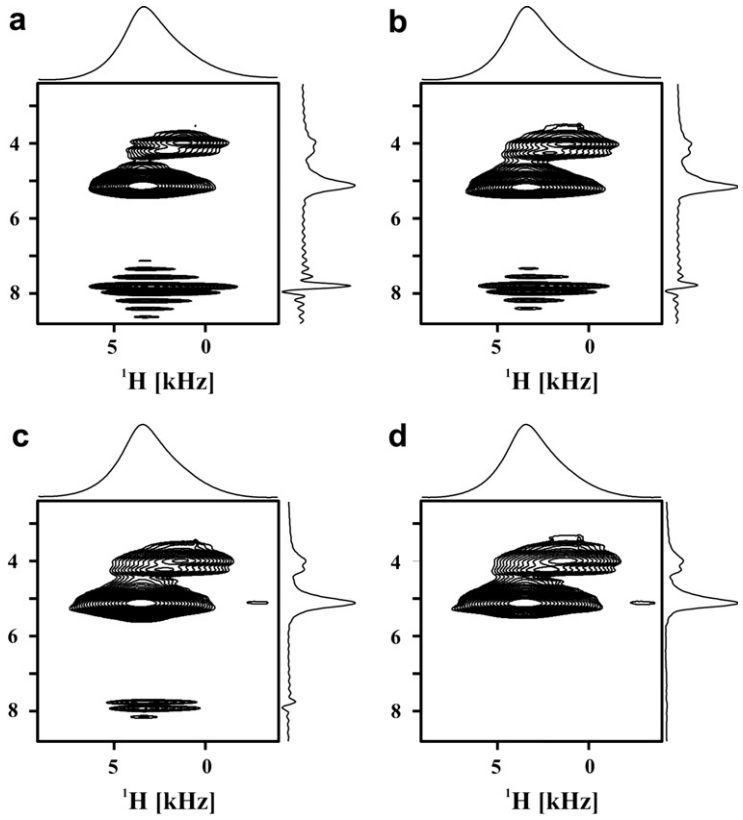

Fig. 9. 2D ^{1}H{FSLG}–^{1}H HOMCOR spectra of glycine recorded with different θ_m pulse lengths (Fig. 1e). The different θ_m pulse lengths used were: (a) 2.5 μs, (b) 2.1 μs, (c) 1.7 μs and (d) 1.5 μs.

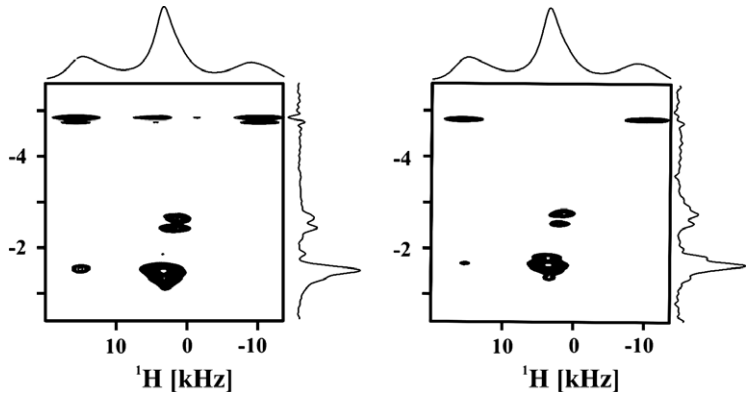

Fig. 10. 2D ^{1}H{PMLG}–^{1}H HOMCOR spectra of glycine recorded with different θ_m pulse lengths (Fig. 1f). The different θ_m pulse lengths used were: (a) 2 μs and (b) 1.5 μs.

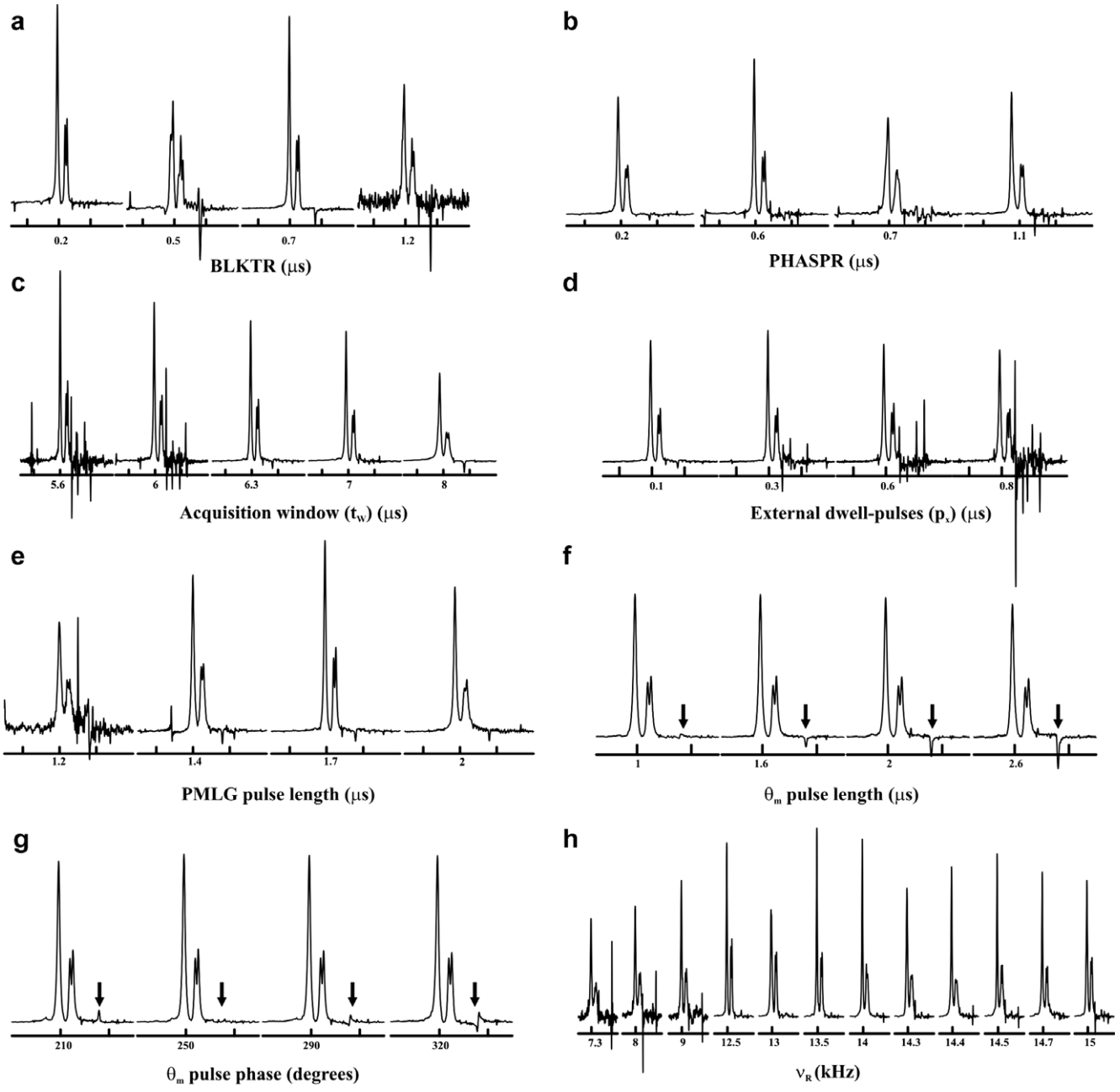

Fig. 11. The influence of the (a) transmitter blanking pulse (*BLKTR*), (b) phase presetting (*PHASPR*), (c) acquisition window t_w, (d) external dwell-pulse p_x, (e) PMLG unit pulse length, (f) θ_m pulse length, (g) θ_m pulse phase and (h) rotation frequency, ν_r (kHz) on 1D *w*PMLG–^{1}H MAS spectra of glycine sample using pulse sequence of Fig. 2g.

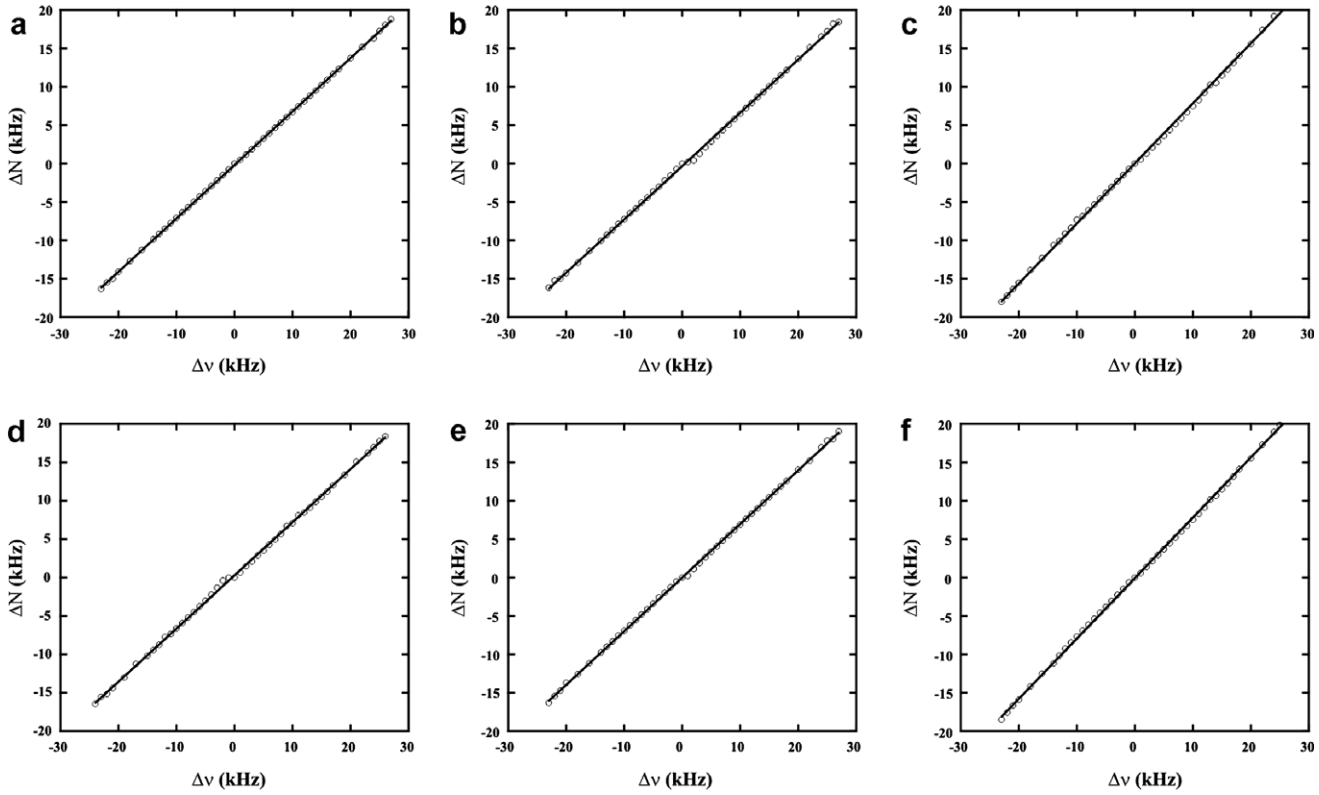

Fig. 12. The effective off-resonance values ΔN (kHz) as a function of the actual chemical shift $\Delta\nu$ (kHz) for different ^{1}H *wPMLG5* decoupling schemes: (a) *wPMLG5*$^-$, (b) $w\overline{PMLG5}^-$, (c) *wPMLG5*$^-$, $w\overline{PMLG5}^-$, (d) *wPMLG5*$^+$, (e) $w\overline{PMLG5}^+$ and (f) *wPMLG5*$^+$, $w\overline{PMLG5}^+$.

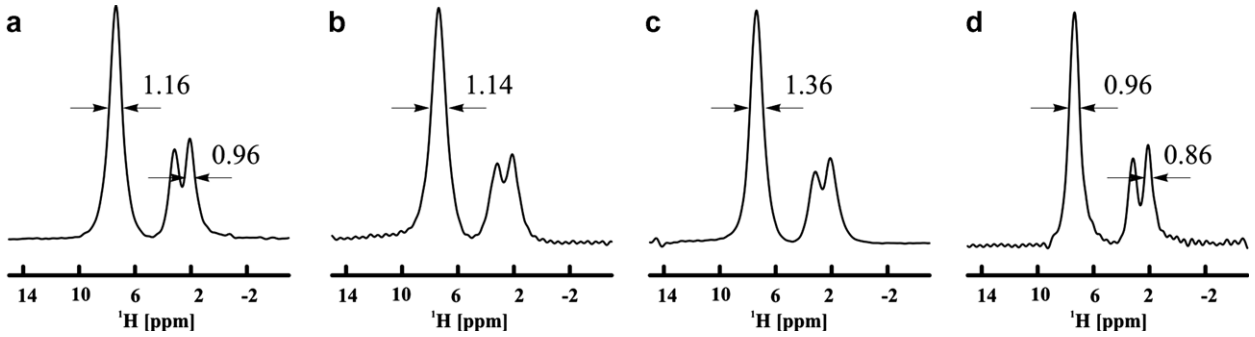

Fig. 13. ^{1}H MAS NMR spectra of glycine obtained using the different ^{1}H *w*PMLG5 varants: (a) *wPMLG5*$^-$, (b) *wPMLG5*$^+$, (c) $w\overline{PMLG5}^+$, (d) $w\overline{PMLG5}^-$. The linewidths (in ppm) are depicted on the figures for comparison.

are found between *wPMLG5*$^+$ and its complementary variant $w\overline{PMLG5}^+$ in terms of efficiency. Although it has been shown that combining both variants in a supercycle scheme with the form *wPMLG5*$^{\pm}w\overline{PMLG5}^{\pm}$, improved ^{1}H spectra in terms of artifacts, which afford an effective *z*-rotation in the rotating frame [25]. Our DSX spectrometer does not allow such combination between *wPMLG5*$^{\pm}$ and $w\overline{PMLG5}^{\pm}$ because each one has distinct *BLKTR* and sometimes *PHASPR* values precluding their use as a supercycle (Figure S2a–e). Compared to *w*PMLG*5* variant (Fig. 13a–d), completely optimized for all the experimental parameters, the $w\overline{PMLG5}^-$ decoupling scheme seems to offer an overall resolution improvement.

4.3.7. Sample restricted to the central part of the rotor

Fig. 14 compares the glycine ^{1}H MAS spectra obtained with *w*PMLG*5*$^-$ and with the sample confined or not to the central part of the rotor (12 μl of sample volume). As far as spectral resolution is concerned, no significant differences are observed, though care-

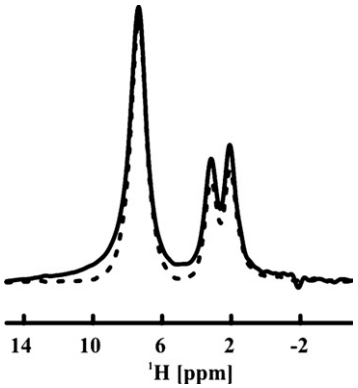

Fig. 14. ^{1}H *wPMLG5*$^-$ spectra of glycine confined (a) or not (b) to the center of the rotor (12 μl of sample volume). The linewidths (in ppm) of the strongly coupled protons are indicated in the figures.

ful inspection of the NH_3 line-shape shows that the resonance is narrower at the baseline, i.e., a slightly better Gaussian shape is obtained when the sample is restricted to the central part of the rotor (Fig. 14, dotted line).

4.4. Comparing the ^1H–^1H decoupling performance of FSLG, PMLG and wPMLG

Fig. 15 compares the fully optimized LG-based ^1H CRAMPS glycine spectra recorded with *FSLG*, *PMLG5*, and *wPMLG5*, employing the same ^1H decoupling power level ($\nu_1 = 84$ kHz). The PMLG5 scheme affords better ^1H resolution than FSLG (cf. Fig. 15a and b) but the former shows not so clean baseline in comparison with the latter. The same conclusion is reached when comparing the 2D $^1H\{PMLG5\}$-$^1H\{wPMLG5\}$ (Fig. 15c and d) and 2D $^1H\{FSLG\}$-$^1H\{wPMLG5\}$ HOMCOR spectra (Fig. 15e and f). Although dependent on the spectrometer console, the FSLG experiments seems to be easier to implement than the PMLG experiments in older consoles not always able to change pulse phases with a given

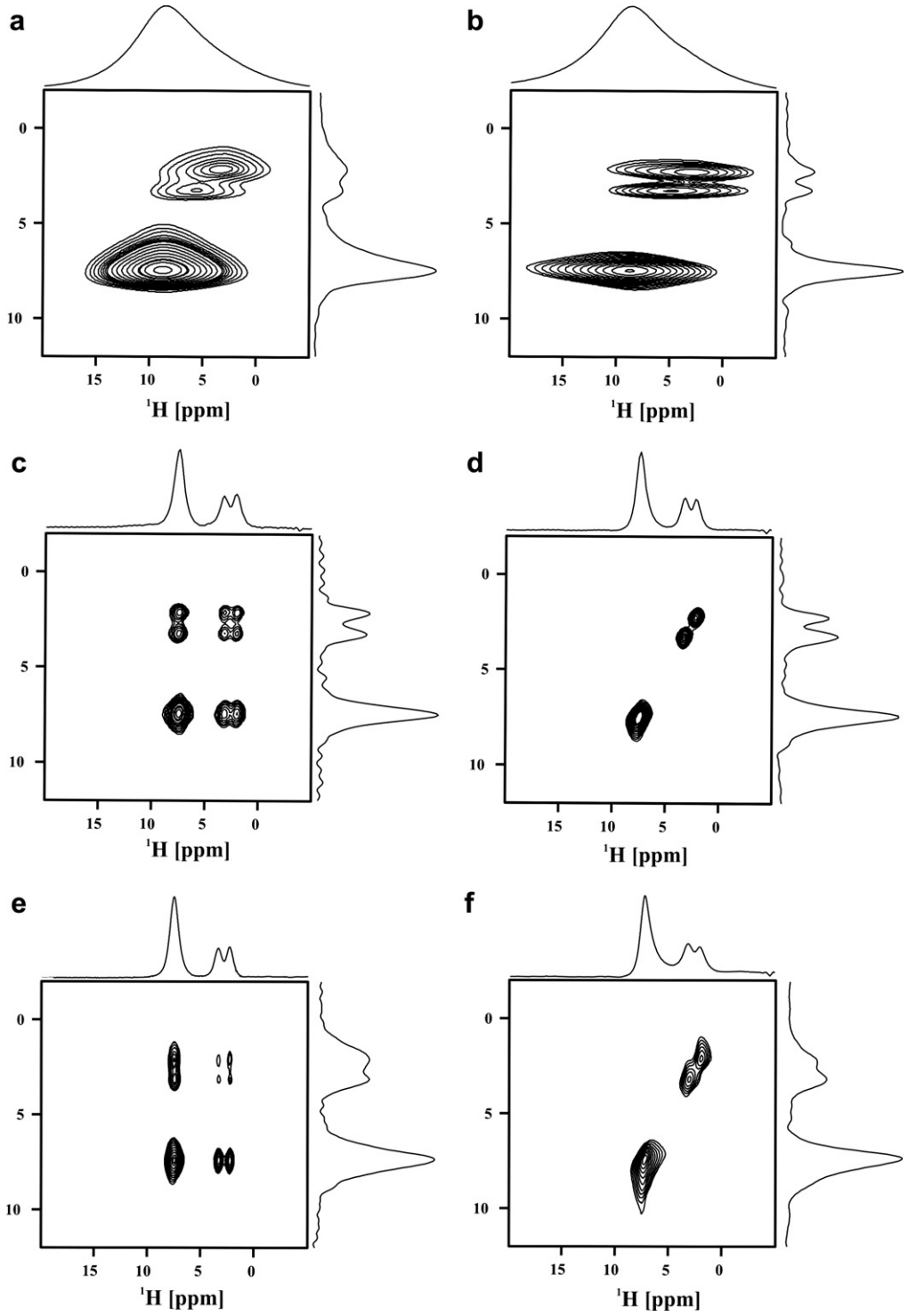

Fig. 15. 2D ^1H MAS NMR spectra of glycine employing: (a) $^1H\{FSLG\}$–^1H HOMCOR, (b) $^1H\{PMLG5\}$–^1H HOMCOR, (c) $^1H\{PMLG5\}$–$^1H\{wPMLG\}$ HOMCOR ($t_m = 500$ μs), (d) $^1H\{PMLG5\}$–$^1H\{wPMLG5\}$ HOMCOR ($t_m = 2$ μs), (e) $^1H\{FSLG\}$–$^1H\{wPMLG5\}$ HOMCOR ($t_m = 500$ μs) and (f) $^1H\{FSLG\}$–$^1H\{wPMLG5\}$ HOMCOR ($t_m = 2$ μs).

phase increment along $n \times 10$ consecutive pulses (for the case of PMLG5).

The windowed PMLG5 based 2D experiments have shown a remarkable performance on both dimensions in terms of ^{1}H resolution. PMLG or FSLG decoupling blocks may be easily placed during t_1, while a windowed acquisition using wPMLG5 may be applied during t_2. In such sequences (Fig. 1g–i) the wPMLG5 block must be carefully optimized as discussed above, by running several 1D wPMLG5 experiments. Essentially, the different ^{1}H CRAMPS variants shown here may be chosen according to: (i) the ^{1}H region to be enhanced in terms of resolution (ii) the possibility to implement them because such techniques are strongly depend on the spectrometer console and probe characteristics since fast changes in phase or frequency are required. For further details concerning additional insights into homonuclear decoupling, a theoretical comparison between FSLG, PMLG, and DUMBO homonuclear decoupling sequences was very recently reported [84]. In that work numerical simulations applied on such decoupling schemes are used to explore the interaction between the magic-angle spinning and *rf* decoupling, the effects of tilt pulses in acquisition windows and the effects of phase propagation delay on tilted axis precession.

4.5. Application of ^{1}H CRAMPS techniques to organic and inorganic–organic materials

In this second part, the aim is to demonstrate the robustness and usefulness of ^{1}H CRAMPS LG-based decoupling techniques for the study of 'real' systems, such as organic and inorganic–organic hybrid materials. Three compounds have been studied: compound **I** (Fig. 16) previously used in the synthesis of interesting materials, material **II**, which consists of a three-dimensional mixed-metal framework (Fig. 17) incorporating **I** and 4,4′-bipyridine, and **III** an organically templated titanium phosphate (Fig. 18). A simple structural description of such materials is reported below followed by the study of the hydrogen bonding networks involved in such systems, by ^{1}H CRAMPS. Our aim is not the comprehensive attribution of the ^{1}H resonances, which has been discussed elsewhere [33,72], but to demonstrate and compare the ability of the different ^{1}H CRAMPS decoupling techniques to resolve ^{1}H resonances in these systems.

4.5.1. H_4 pmida (*I*) and the germanium binuclear complex (*II*)

FSLG, PMLG5 and wPMLG5^{1}H were tested on **I** (Fig. 19a–d) and **II** (Fig. 20a–c). A maximum of six and four ^{1}H resonances were resolved in **I** (Fig. 19a and b) and **II** (Fig. 20a–c), respectively. Some similarity between the spectra of **I** and **II** are observed in the range δ = 3.0–5.5 ppm, attributed to CH_2 groups. The resonances of the protonated amine groups ($^+$N–H) are easily resolved in the spectra of **I** and **II**, at ca. 8.2 and 8.8 ppm, respectively. For **I**, the peaks at ca. 13.8 and 11.5 ppm are assigned to PO–H···OP and CO–H···OP/N^+–H···OP, respectively (Fig. 19b). For **II**, the 2D ^{1}H{FSLG}–^{1}H{*w*PMLG} HOMCOR experiment shows a resolved peak at ca. 7.1 ppm tentatively assigned to Ge–OH groups (Fig. 20b). All the three decoupling techniques afforded similar resolution, considerably better

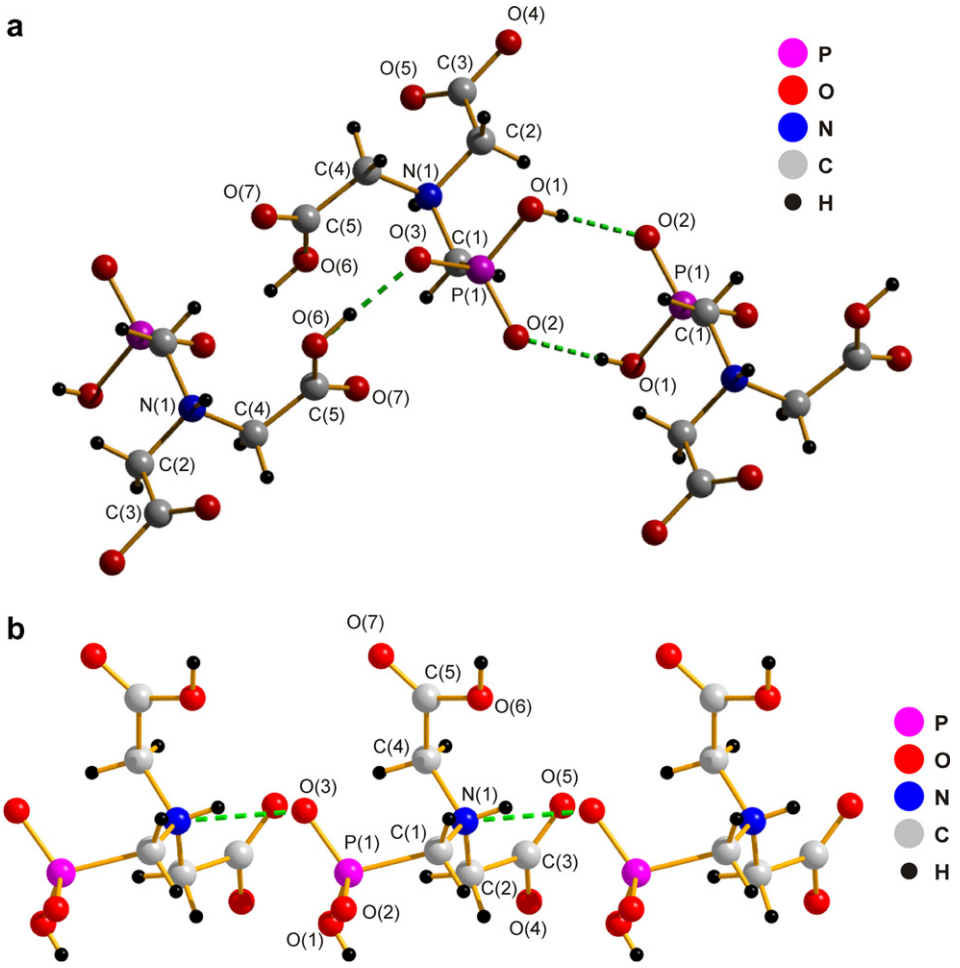

Fig. 16. Hydrogen-bonding environments of I emphasized with green dashed lines viewed along (a) the *a*-axis and (b) *b*-axis. Colour codes are: P (pink); O (red); C (gray); N (blue); H (white). (For interpretation of the references in colour in this figure legend, the reader is referred to the web version of this article.)

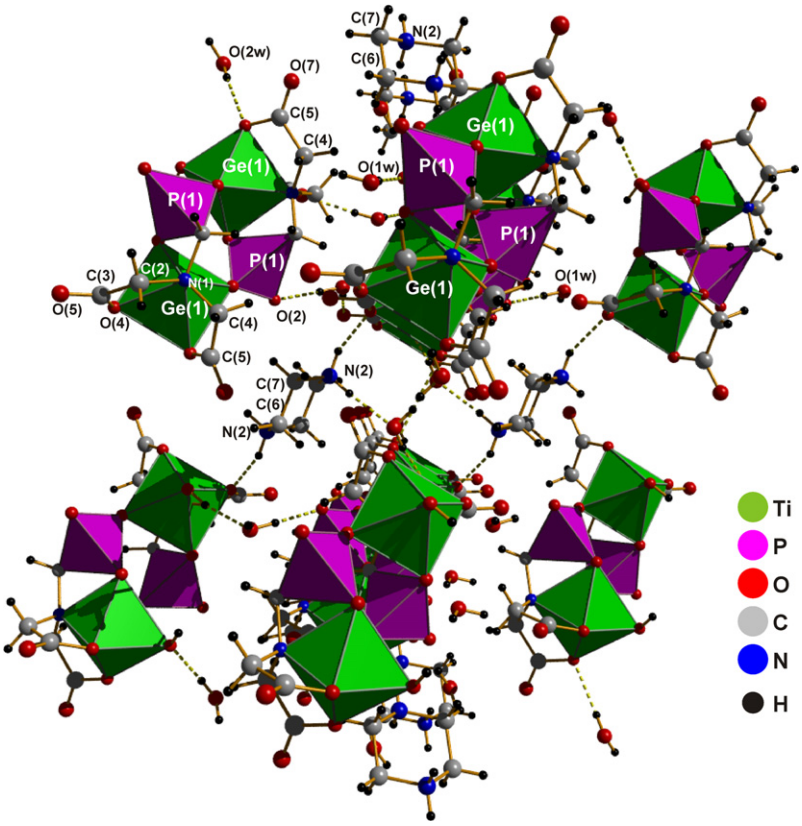

Fig. 17. Crystal structure of II viewed along the [1 1 0] direction [33]. The green dashed lines emphasize the hydrogen-bonding network involving water, piperazinium cations and the binuclear complex, $Ge_2[(pmida)_2(OH)_2]^{2-}$. The compound contains an anionic binuclear complex, $Ge_2[(pmida)_2(OH)_2]^{2-}$. The $pmida^{4-}$ ion appears as a polydentate organic ligand, which completely traps the Ge^{4+} inside three distinct five-membered chelate rings formed by the two carboxylate and phosphonate groups connected in a typical anti-unidentate coordinative fashion. Ge^{4+} center in the anionic $[Ge_2(pmida)_2(OH)_2]^{2-}$ complex is coordinated to two $pmida^{4-}$ ligand and to a hydroxyl group Ge–OH. The change of the anionic complex is compensated by the presence of piperazinedium cations, $C_4H_{12}N_{22}^{+}$, which, long with the two water of crystallization molecules, exhibit strong and highly directional hydrogen bonds with the anionic $[Ge_2(pmida)_2(OH)_2]^{2-}$ complex. Colour codes are: Ge (green polyhedra); P (pink polyhedra); O (red ball); C (gray ball); N (blue); H (white ball). (For interpretation of the references in colour in this figure legend, the reader is referred to the web version of this article.)

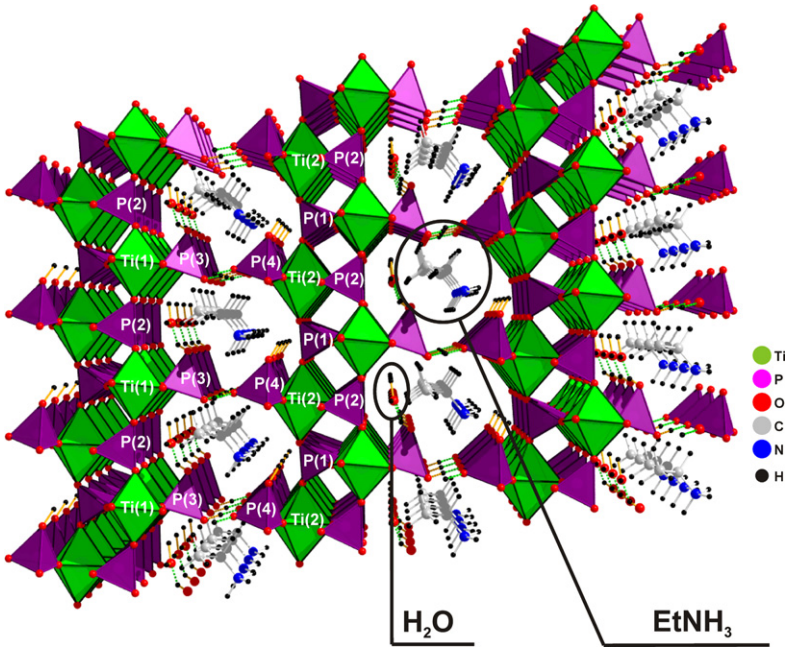

Fig. 18. Crystal structure of III [72]. The $(C_2H_5NH_3)[Ti(H_{1.5}PO_4)(PO_4)]_2{\cdot}H_2O$ complex has been formed by the hydrothermal reaction between $TiCl_4$, phosphoric acid H_3PO_4 and ethylamine. This complex is constituted by elongated plates of homogeneous size. In this intercalation compound, individual two-dimensional anionic $[Ti(HPO_4)(PO_4)]^{-}$ sheets formed by $\{PO_4\}$ tetrahedral and $\{TiO_6\}$ octahedral. The structure contains two kinds of phosphate groups: PO_4^{3-} sharing their oxygen atoms with titanium centers, and HPO_4^{2-} having two bridging and two terminal oxygen atoms. These terminal HPO_4^{2-} groups are connected to the chains and point towards the interlayer region, directly interacting with the protonated amine groups from neighboring *n*-hexylammonium cations through hydrogen bond. Colour codes are depicted in the figure. (For interpretation of the references in colour in this figure legend, the reader is referred to the web version of this article.)

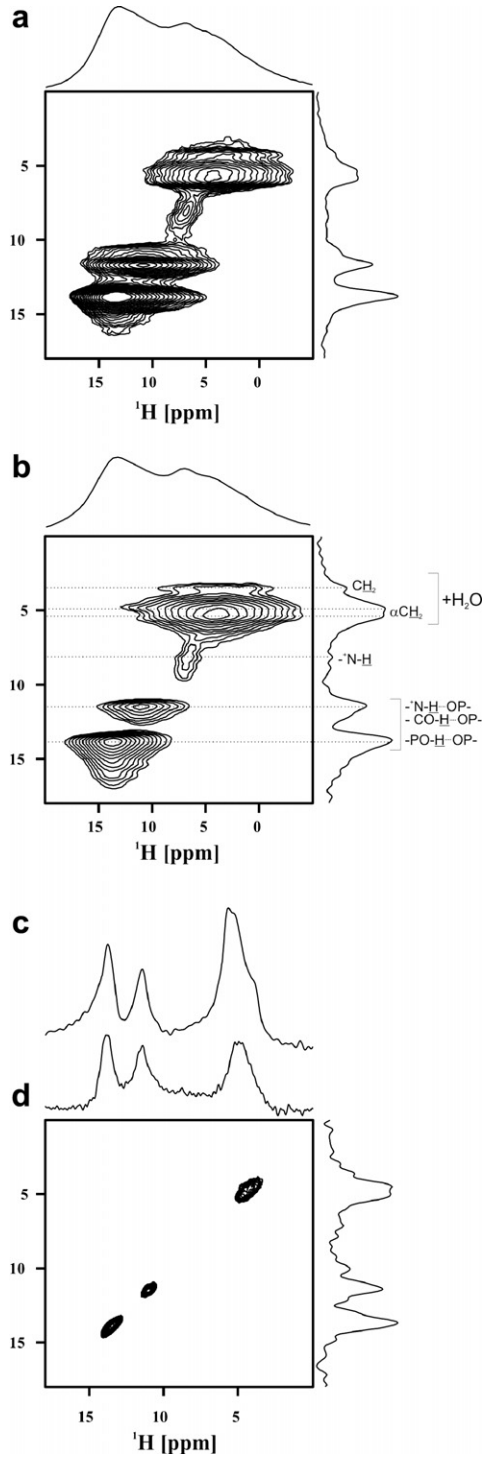

Fig. 19. 2D ^{1}H MAS NMR spectra of I employing (a) 2D ^{1}H{FSLG}–^{1}H HOMCOR, (b) 2D ^{1}H{PMLG5}–^{1}H HOMCOR, (c) 1D *w*PMLG5 and (d) 2D ^{1}H{FSLG}–^{1}H{*w*PMLG5} HOMCOR experiments. ^{1}H peak assignment is depicted in (b).

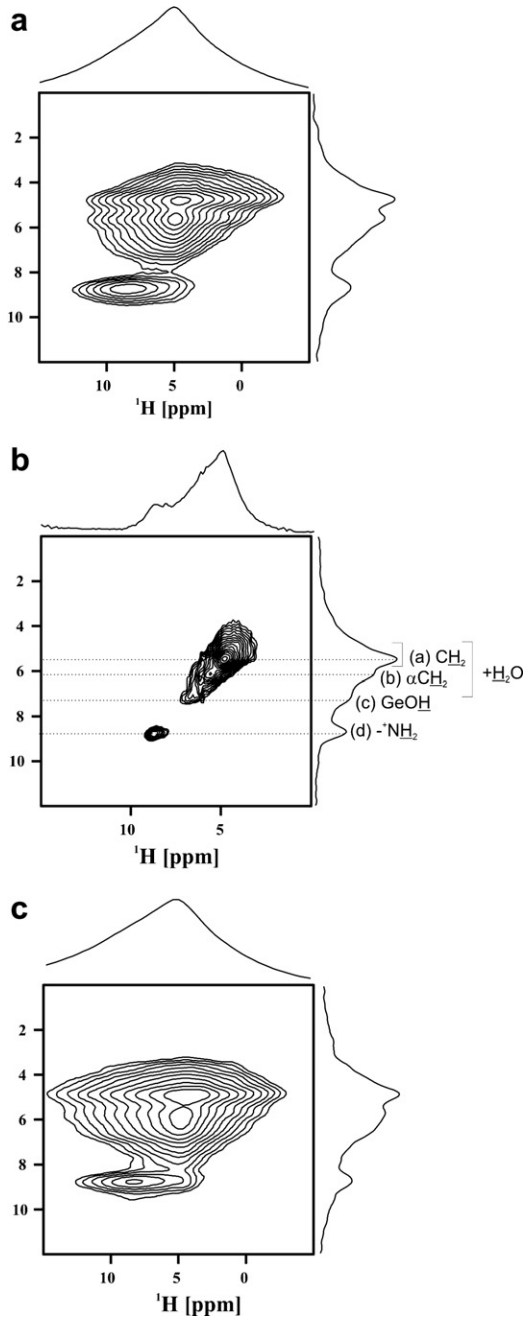

Fig. 20. 2D ^{1}H MAS NMR spectra of II employing 2D (a) ^{1}H{FSLG}–^{1}H, (b) ^{1}H{FSLG}–^{1}H{*w*PMLG} and (c) ^{1}H{PMLG}–^{1}H HOMCOR experiments.

than the simple ^{1}H MAS spectra. The 2D wPMLG5 spectra (Fig. 19c and d) display high resolution in both dimensions.

In the case of **I**, the ^{1}H CRAMPS performance is put in evidence, in particular, in the 3.0–5.5 ppm region. Using the conditions previously optimized on glycine and adamantane, all the ^{1}H spectra recorded with the three CRAMPS variants (Fig. 19a–d) allow the clear distinction of the two distinct CH_2 groups (which were barely resolved in our original work [33]).

It is interesting to compare ^{1}H CRAMPS and ^{1}H fast MAS (ν_R = 30 kHz) spectra. Whereas the latter (Fig. 21a) displays broad and featureless peak the former (Fig. 21b and c) exhibit a significant resolution improvement.

*4.5.2. Intercalated layered γ-titanium phosphate (**III**)*

The ^{1}H MAS spectrum of **III** (shown in [72]) consists of a broad peak between 0 and 10 ppm. Fig. 22a–c shows the 2D spectra obtained by ^{1}H CRAMPS decoupling in both dimensions and reveals that both FSLG and PMLG decoupling afford similar resolution enhancement, with seven ^{1}H peaks being observed. The resonances at ca. 1.6, 3.2 and 6.8 ppm are attributed to CH_3, CH_2 and the NH of the ethylammonium cation, $C_2H_5NH_3^+$. Two P-OH resonances at ca. 7.6 and 9.4 ppm are well resolved [33]. A third POH environment,

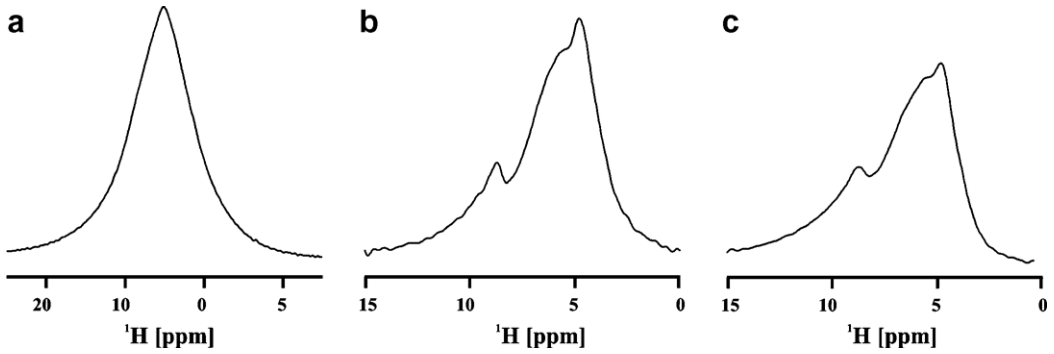

Fig. 21. Comparing the ^{1}H resolution on II using (a) ^{1}H fast MAS (ν_r = 30 kHz) and (b–c) ^{1}H wPMLG5 [(b) ν_r = 12.5 kHz, (c) ν_r = 14 kHz] experiments.

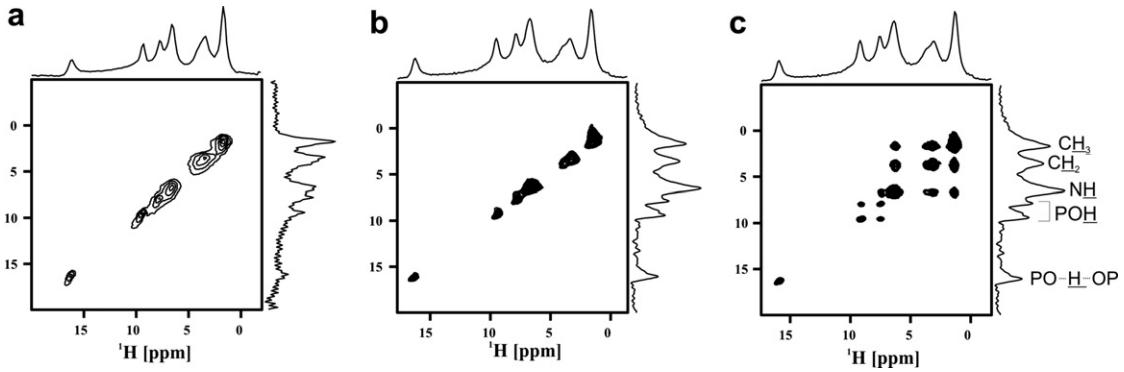

Fig. 22. 2D ^{1}H MAS NMR spectra of III employing (a) ^{1}H{PMLG5}–^{1}H{*w*PMLG5} HOMCOR, (b) ^{1}H{FSLG}–^{1}H{*w*PMLG5} HOMCOR (t_m = 2 μs) and (c) ^{1}H{FSLG}–^{1}H {*w*PMLG5} HOMCOR (t_m = 500 μs).

at ca. 16.2 ppm, is attributed to the strong PO···H···OP hydrogen bond between two inorganic titanium-phosphates. In addition, ^{1}H–^{1}H decoupling allowed the discrimination of the two ^{1}H resonances from the CH_2 group, which may be observed by the splitting centered at ca. 3.2 ppm. It is worth mentioning that the F1 dimension, of the ^{1}H spectrum recorded with PMLG5 (Fig. 22a), is noisier than the corresponding spectrum recorded with FSLG decoupling (Fig. 22b and c). Although all these 2D ^{1}H spectra were recorded using the best conditions derived from optimization on glycine, PMLG needs further fine-tuning for best performance.

5. Conclusion

In this work, several practical aspects of the implementation of LG-based ^{1}H CRAMPS techniques have been addressed. We hope that this will assist chemists and materials scientists in their efforts to apply these very useful methods in the study of their samples. The influence of parameters such as pulse lengths, *rf* offset, *rf* field strength, spectrometer constants, among others, on 1D and 2D ^{1}H spectra have been discussed, involving windowless (FSLG and PMLG*5*) and windowed (*w*PMLG*5*) ^{1}H–^{1}H decoupling techniques. Special attention was given to the influence of the different parameters of ^{1}H CRAMPS experiments on the ^{1}H chemical shift scaling factor because having the correct chemical shift scale is of paramount importance for resonance assignment.

The comparison between the three ^{1}H homonuclear decoupling schemes revealed that each one has its own advantages, depending on the hardware specifications and on the pulse sequence used to retrieve chemical information. Before carrying out ^{1}H-X HETCOR experiments it is very useful to first optimize the windowless ^{1}H–^{1}H decoupling block using a 2D ^{1}H{CRAMPS}–^{1}H HOMCOR experiment, in order to obtain the best resolution possible and the correct scaling factor. Such strategy helps tuning the HETCOR variant because some ^{1}H peaks may disappear in ^{1}H-X HETCOR experiments if no ^{1}H nuclei are in close proximity of a given X nuclei, for example. This may complicate the chemical shift calibration. On the other hand, for routine analysis, *w*PMLG*n* is a very useful experiment if a quick high-resolution ^{1}H spectrum is required. This windowed technique allows a preliminary selection of the desired samples before using more sophisticated 2D ^{1}H CRAMPS methods. The same idea may be is equally true for wDUMBO [27].

In the near future, combining periodic *rf* multiple pulse sequences with already available ultra fast spinning (up to 70 kHz) poses new challenges to ^{1}H CRAMPS. This combination will be especially useful for ^{1}H–^{1}H DQ recoupling experiments where high spinning rates are needed to eliminate, as much as possible, ^{1}H dipolar couplings in order to recouple ^{1}H spins with better performance. In addition, ^{1}H windowless multiple-pulse schemes may help between the DQ excitation and reconversion steps, while windowed ^{1}H acquisition schemes in obtaining a highly resolved DQ ^{1}H indirect dimension. This has already been successfully applied for moderate spinning speeds, [27,77,86]. Windowed ^{1}H acquisition schemes have the advantage of affording highly resolved ^{1}H spectra in a single dimension, thus opening the possibility to be used during t_2 evolution in other 2D pulse schemes where high-resolution ^{1}H detection may help performing insensitive experiments by applying inverse detection experiments. A comparison study applied between all the recent ^{1}H–^{1}H decoupling schemes is underway on the most modern NMR consoles available nowadays at high magnetic fields.

Acknowledgments

This research was supported by CICECO and University of Aveiro. We also thank Fundação para a Ciência e Tecnologia (FCT) for

their general financial support and for the Post-Doc Grant SFRH/BPD/34136/2006 (to C. Coelho).

Supplementary data

Supplementary data associated with this article can be found, in the online version, at doi:10.1016/j.jmr.2008.07.019.

References

[1] B. Reif, C.P. Jaroniec, C.M. Rienstra, M. Hohwy, R.G. Griffin, H-1-H-1 MAS correlation spectroscopy and distance measurements in a deuterated peptide, J. Magn. Reson. 151 (2001) 320–327.
[2] I. Schnell, S.P. Brown, H.Y. Low, H. Ishida, H.W. Spiess, An investigation of hydrogen bonding in benzoxazine dimers by fast magic-angle spinning and double-quantum H-1 NMR spectroscopy, J. Am. Chem. Soc. 120 (1998) 11784–11795.
[3] I. Schnell, H.W. Spiess, High-resolution H-1 NMR spectroscopy in the solid state: very fast sample rotation and multiple-quantum coherences, J. Magn. Reson. 151 (2001) 153–227.
[4] S.P. Brown, I. Schnell, J.D. Brand, K. Mullen, H.W. Spiess, An investigation of pi-pi packing in a columnar hexabenzocoronene by fast magic-angle spinning and double-quantum H-1 solid-state NMR spectroscopy, J. Am. Chem. Soc. 121 (1999) 6712–6718.
[5] R.K. Harris, P. Jackson, L.H. Merwin, B.J. Say, G. Hagele, Perspectives in high-resolution solid-state nuclear magnetic-resonance, with emphasis on combined rotation and multiple-pulse spectroscopy, J. Chem. Soc.—Faraday Trans. I 84 (1988) 3649–3672.
[6] J.W. Traer, E. Montoneri, A. Samoson, J. Past, T. Tuherm, G.R. Goward, Unraveling the complex hydrogen bonding of a dual-functionality proton conductor using ultrafast magic angle spinning NMR, Chem. Mater. 18 (2006) 4747–4754.
[7] P. Mansfiel, Symmetrized pulse sequences in high resolution Nmr in solids, J. Phys. C Solid State Phys. 4 (1971) 1444–1452.
[8] W.K. Rhim, D.D. Elleman, R.W. Vaughan, Analysis of multiple pulse Nmr in solids, J. Chem. Phys. 59 (1973) 3740–3749.
[9] J.S. Waugh, L.M. Huber, U. Haeberle, Approach to high-resolution Nmr in solids, Phys. Rev. Lett. 20 (1968) 180–182.
[10] D.G. Cory, A new multiple-pulse cycle for homonuclear dipolar decoupling, J. Magn. Reson. 94 (1991) 526–534.
[11] D.P. Burum, M. Linder, R.R. Ernst, Low-power multipulse line narrowing in solid-state Nmr, J. Magn. Reson. 44 (1981) 173–188.
[12] M. Hohwy, P.V. Bower, H.J. Jakobsen, N.C. Nielsen, A high-order and broadband CRAMPS experiment using *z*-rotational decoupling, Chem. Phys. Lett. 273 (1997) 297–303.
[13] A. Bielecki, A.C. Kolbert, M.H. Levitt, Frequency-switched pulse sequences—homonuclear decoupling and dilute spin Nmr in solids, Chem. Phys. Lett. 155 (1989) 341–346.
[14] B.J. vanRossum, H. Forster, H.J.M. deGroot, High-field and high-speed CP-MAS C-13 NMR heteronuclear dipolar-correlation spectroscopy of solids with frequency-switched Lee–Goldburg homonuclear decoupling, J. Magn. Reson. 124 (1997) 516–519.
[15] M. Mehring, J.S. Waugh, Magic-angle NMR experiments in solids, Phys. Rev. B 5 (1972) 3459–3471.
[16] E. Vinogradov, P.K. Madhu, S. Vega, High-resolution proton solid-state NMR spectroscopy by phase-modulated Lee–Goldburg experiment, Chem. Phys. Lett. 314 (1999) 443–450.
[17] E. Vinogradov, P.K. Madhu, S. Vega, A bimodal Floquet analysis of phase modulated Lee–Goldburg high resolution proton magic angle spinning NMR experiments, Chem. Phys. Lett. 329 (2000) 207–214.
[18] E. Vinogradov, P.K. Madhu, S. Vega, Phase modulated Lee–Goldburg magic angle spinning proton nuclear magnetic resonance experiments in the solid state: a bimodal Floquet theoretical treatment, J. Chem. Phys. 115 (2001) 8983–9000.
[19] A. Lesage, D. Sakellariou, S. Hediger, B. Elena, P. Charmont, S. Steuernagel, L. Emsley, Experimental aspects of proton NMR spectroscopy in solids using phase-modulated homonuclear dipolar decoupling, J. Magn. Reson. 163 (2003) 105–113.
[20] D. Sakellariou, A. Lesage, P. Hodgkinson, L. Emsley, Homonuclear dipolar decoupling in solid-state NMR using continuous phase modulation, Chem. Phys. Lett. 319 (2000) 253–260.
[21] B. Elena, G. de Paepe, L. Emsley, Direct spectral optimisation of proton–proton homonuclear dipolar decoupling in solid-state NMR, Chem. Phys. Lett. 398 (2004) 532–538.
[22] D.P. Burum, W.K. Rhim, Analysis of multiple pulse Nmr in Solids. 3, J. Chem. Phys. 71 (1979) 944–956.
[23] D.P. Burum, W.K. Rhim, Improved Nmr technique for homonuclear dipolar decoupling in solids—application to polycrystalline ice, J. Chem. Phys. 70 (1979) 3553–3554.
[24] L. Bosman, P.K. Madhu, S. Vega, E. Vinogradov, Improvement of homonuclear dipolar decoupling sequences in solid-state nuclear magnetic resonance utilising radiofrequency imperfections, J. Magn. Reson. 169 (2004) 39–48.
[25] M. Leskes, P.K. Madhu, S. Vega, Proton line narrowing in solid-state nuclear magnetic resonance: new insights from windowed phase-modulated Lee–Goldburg sequence, J. Chem. Phys. 125 (2006) 124506–124518.
[26] M.H. Levitt, A.C. Kolbert, A. Bielecki, D.J. Ruben, High-resolution H-1-Nmr in solids with frequency-switched multiple-pulse sequences, Solid State Nucl. Magn. Reson. 2 (1993) 151–163.
[27] S.P. Brown, A. Lesage, B. Elena, L. Emsley, Probing proton-proton proximities in the solid state: high-resolution two-dimensional H-1-H-1 double-quantum CRAMPS NMR spectroscopy, J. Am. Chem. Soc. 126 (2004) 13230–13231.
[28] P.K. Madhu, X. Zhao, M.H. Levitt, High-resolution H-1 NMR in the solid state using symmetry-based pulse sequences, Chem. Phys. Lett. 346 (2001) 142–148.
[29] S. Paul, R.S. Thakur, P.K. Madhu, 1H homonuclear dipolar decoupling at high magic-angle spinning frequencies with rotor-synchronised symmetry sequences, Chem. Phys. Lett. 456 (2008) 253–256.
[30] Y.F. Wei, D.K. Lee, A.E. McDermott, A. Ramamoorthy, A 2D MAS solid-state NMR method to recover the amplified heteronuclear dipolar and chemical shift anisotropic interactions, J. Magn. Reson. 158 (2002) 23–35.
[31] Y.F. Wei, D.K. Lee, A. Ramamoorthy, One-dimensional dipolar-shift spectroscopy under magic angle spinning to determine the chemical-shift anisotropy tensors, Chem. Phys. Lett. 324 (2000) 20–24.
[32] A. Lesage, L. Duma, D. Sakellariou, L. Emsley, Improved resolution in proton NMR spectroscopy of powdered solids, J. Am. Chem. Soc. 123 (2001) 5747–5752.
[33] L. Mafra, F.A.A. Paz, F.N. Shi, J. Rocha, T. Trindade, C. Fernandez, A. Makal, K. Wozniak, J. Klinowski, X-ray diffraction and solid-state NMR studies of a germanium binuclear complex, Chem. Eur. J. 12 (2005) 363–375.
[34] L. Mafra, J. Rocha, C. Fernandez, F.A.A. Paz, Characterization of microporous aluminophosphate IST-1 using H-1 Lee–Goldburg techniques, J. Magn. Reson. 180 (2006) 236–244.
[35] A. Lesage, S. Steuernagel, L. Emsley, Carbon-13 spectral editing in solid-state NMR using heteronuclear scalar couplings, J. Am. Chem. Soc. 120 (1998) 7095–7100.
[36] B.J. van Rossum, F. Castellani, J. Pauli, K. Rehbein, J. Hollander, H.J.M. de Groot, H. Oschkinat, Assignment of amide proton signals by combined evaluation of HN, NN and HNCA MAS-NMR correlation spectra, J. Biomol. NMR 25 (2003) 217–223.
[37] B.J. van Rossum, C.P. de Groot, V. Ladizhansky, S. Vega, H.J.M. de Groot, A method for measuring heteronuclear (H-1-C-13) distances in high speed MAS NMR, J. Am. Chem. Soc. 122 (2000) 3465–3472.
[38] J. Brus, A. Jegorov, Through-bonds and through-space solid-state NMR correlations at natural isotopic abundance: signal assignment and structural study of simvastatin, J. Phys. Chem. A 108 (2004) 3955–3964.
[39] M. Hong, X.L. Yao, K. Jakes, D. Huster, Investigation of molecular motions by Lee–Goldburg cross-polarization NMR spectroscopy, J. Phys. Chem. B 106 (2002) 7355–7364.
[40] V. Ladizhansky, S. Vega, Polarization transfer dynamics in Lee–Goldburg cross polarization nuclear magnetic resonance experiments on rotating solids, J. Chem. Phys. 112 (2000) 7158–7168.
[41] A. Ramamoorthy, C.H. Wu, S.J. Opella, Experimental aspects of multidimensional solid-state NMR correlation spectroscopy, J. Magn. Reson. 140 (1999) 131–140.
[42] T. Narasimhaswamy, D.K. Lee, K. Yamamoto, N. Somanathan, A. Ramamoorthy, A 2D solid-state NMR experiment to resolve overlapping aromatic resonances of thiophene-based nematogens, J. Am. Chem. Soc. 127 (2005) 6958–6959.
[43] K. Yamamoto, V.L. Ermakov, D.K. Lee, A. Ramamoorthy, PITANSEMA-MAS, a solid-state NMR method to measure heteronuclear dipolar couplings under MAS, Chem. Phys. Lett. 408 (2005) 118–122.
[44] A. Ramamoorthy, C.H. Wu, S.J. Opella, Magnitudes and orientations of the principal elements of the H-1 chemical shift, H-1-N-15 dipolar coupling, and N-15 chemical shift interaction tensors in N-15(epsilon 1)-tryptophan and N-15(pi)-histidine side chains determined by three-dimensional solid-state NMR spectroscopy of polycrystalline samples, J. Am. Chem. Soc. 119 (1997) 10479–10486.
[45] A. Ramamoorthy, Y.F. Wei, D.K. Lee, PISEMA solid-state NMR spectroscopy, Advances in Solid State NMR Studies of Materials and Polymers: A Special Volume Dedicated to Isao Ando 52 (2004) 1–52.
[46] V. Brodski, R. Peschar, H. Schenk, A. Brinkmann, E.R.H. van Eck, A.P.M. Kentgens, B. Coussens, A. Braam, Structure of melaminium dihydrogenpyrophosphate and its formation from melaminium dihydrogenphosphate studied with powder diffraction data, solid-state NMR, and theoretical calculations, J. Phys. Chem. B 108 (2004) 15069–15076.
[47] D.H. Brouwer, J.A. Ripmeester, Symmetry-based recoupling of proton chemical shift anisotropies in ultrahigh-field solid-state NMR, J. Magn. Reson. 185 (2007) 173–178.
[48] S.V. Dvinskikh, Z. Luz, H. Zimmermann, A. Maliniak, D. Sandstrom, Molecular characterization of hexaoctyloxy-rufigallol in the solid and columnar phases: a local field NMR study, J. Phys. Chem. B 107 (2003) 1969–1976.
[49] R. Frantz, J.O. Durand, F. Carre, G.F. Lanneau, J. Le Bideau, B. Alonso, D. Massiot, Synthesis and solid-state NMR studies of P-vinylbenzylphosphonic acid, Chem. Eur. J. 9 (2003) 770–775.
[50] R.Q. Fu, Measurement of N-15-H-1 bond lengths by rotational-echo double-resonance NMR spectroscopy, Chem. Phys. Lett. 376 (2003) 62–67.
[51] A. Lesage, L. Emsley, Through-bond heteronuclear single-quantum correlation spectroscopy in solid-state NMR, and comparison to other through-bond and through-space experiments, J. Magn. Reson. 148 (2001) 449–454.

[52] M. Marjanska, F. Castiglione, J.D. Walls, A. Pines, Measurement of dipolar couplings in partially oriented molecules by local field NMR spectroscopy with low-power decoupling, J. Magn. Reson. 158 (2002) 52–59.
[53] G. Piedra, J.J. Fitzgerald, N. Dando, S.F. Dec, G.E. Maciel, Solid-state H-1 NMR studies of aluminum oxide hydroxides and hydroxides, Inorg. Chem. 35 (1996) 3474–3478.
[54] D. Sakellariou, A. Lesage, L. Emsley, Proton–proton constraints in powdered solids from H-1-H-1-H-1 and H-1-H-1-C-13 three-dimensional NMR chemical shift correlation spectroscopy, J. Am. Chem. Soc. 123 (2001) 5604–5605.
[55] Z.T. Gu, S.J. Opella, Three-dimensional C-13 shift/H-1-N-15 coupling/N-15 shift solid-state NMR correlation spectroscopy, J. Magn. Reson. 138 (1999) 193–198.
[56] Alia, J. Matysik, I. de Boer, P. Gast, H.J. van Gorkom, H.J.M. de Groot, Heteronuclear 2D (H-1-C-13) MAS NMR resolves the electronic structure of coordinated histidines in light-harvesting complex II: assessment of charge transfer and electronic delocalization effect, J. Biomol. NMR 28 (2004) 157–164.
[57] V. Chevelkov, B.J. van Rossum, F. Castellani, K. Rehbein, A. Diehl, M. Hohwy, S. Steuernagel, F. Engelke, H. Oschkinat, B. Reif, H-1 detection in MAS solid-state NMR spectroscopy of biomacromolecules employing pulsed field gradients for residual solvent suppression, J. Am. Chem. Soc. 125 (2003) 7788–7789.
[58] A.F.L. Creemers, S. Kiihne, P.H.M. Bovee-Geurts, W.J. DeGrip, J. Lugtenburg, H.J.M. de Groot, H-1 and C-13 MAS NMR evidence for pronounced ligand–protein interactions involving the ionone ring of the retinylidene chromophore in rhodopsin, Proceedings of the National Academy of Sciences of the United States of America 99 (2002) 9101–9106.
[59] R.Q. Fu, C.L. Tian, T.A. Cross, NMR spin locking of proton magnetization under a frequency-switched Lee–Goldburg pulse sequence, J. Magn. Reson. 154 (2002) 130–135.
[60] D. Huster, S. Yamaguchi, M. Hong, Efficient beta-sheet identification in proteins by solid-state NMR spectroscopy, J. Am. Chem. Soc. 122 (2000) 11320–11327.
[61] D. Huster, X.L. Yao, M. Hong, Membrane protein topology probed by H-1 spin diffusion from lipids using solid-state NMR spectroscopy, J. Am. Chem. Soc. 124 (2002) 874–883.
[62] H. Kono, T. Erata, M. Takai, Determination of the through-bond carbon–carbon and carbon–proton connectivities of the native celluloses in the solid state, Macromolecules 36 (2003) 5131–5138.
[63] A. Lesage, P. Charmont, S. Steuernagel, L. Emsley, Complete resonance assignment of a natural abundance solid peptide by through-bond heteronuclear correlation solid-state NMR, J. Am. Chem. Soc. 122 (2000) 9739–9744.
[64] K. Murata, H. Kono, E. Katoh, S. Kuroki, I. Ando, A study of conformational stability of polypeptide blends by solid state two-dimensional C-13-H-1 heteronuclear correlation NMR spectroscopy, Polymer 44 (2003) 4021–4027.
[65] B.J. van Rossum, F. Castellani, K. Rehbein, J. Pauli, H. Oschkinat, Assignment of the nonexchanging protons of the alpha-spectrin SH3 domain by two- and three-dimensional H-1-C-13 solid-state magic-angle spinning NMR and comparison of solution and solid-state proton chemical shifts, Chembiochem 2 (2001) 906–914.
[66] K. Yamauchi, S. Kuroki, I. Ando, The amide proton NMR chemical shift and hydrogen-bonded structure of glycine-containing peptides and polypeptides in the solid state as studied by multi-pulse-associated high-speed MAS H-1 NMR, J. Mol. Struct. 602 (2002) 9–16.
[67] X.L. Yao, V.P. Conticello, M. Hong, Investigation of the dynamics of an elastin-mimetic polypeptide using solid-state NMR, Magn. Reson. Chem. 42 (2004) 267–275.
[68] Y.F. Wei, D.K. Lee, K.J. Hallock, A. Ramamoorthy, One-dimensional H-1-detected solid-state NMR experiment to determine amide-H-1 chemical shifts in peptides, Chem. Phys. Lett. 351 (2002) 42–46.
[69] B.J. van Rossum, E.A.M. Schulten, J. Raap, H. Oschkinat, H.J.M. de Groot, A 3-D structural model of solid self-assembled chlorophyll a/H2O from multispin labeling and MAS NMR 2-D dipolar correlation spectroscopy in high magnetic field, J. Magn. Reson. 155 (2002) 1–14.
[70] X.J. Ai, F. Deng, J.X. Dong, W. Hu, H. Xu, C.H. Ye, One- and two-dimensional solid-state magic angle spinning NMR studies on the hydration process of layered sodium disilicate SKS-6, Solid State Nucl. Magn. Reson. 25 (2004) 216–226.
[71] B. Alonso, D. Massiot, Mufti-scale NMR characterisation of mesostructured materials using H-1 → C-13 through-bond polarisation transfer, fast MAS, and H-1 spin diffusion, J. Magn. Reson. 163 (2003) 347–352.
[72] L. Mafra, J. Rocha, C. Fernandez, G.R. Castro, S. García-Granda, A. Espina, S.A. Khainakov, J.R. García, Characterization of layered γ-titanium phosphate (C2H5NH3)[Ti(H1·5PO4)(PO4)]2·H2O intercalate: a combined NMR, synchrotron XRD, and DFT calculations study, Chemistry of Materials (2008).
[73] D. Massiot, B. Alonso, F. Fayon, F. Fredoueil, B. Bujoli, New NMR developments for structural investigation of proton-bearing materials at different length scales, Solid State Sci. 3 (2001) 11–16.
[74] J. Trebosc, J.W. Wiench, S. Huh, V.S.Y. Lin, M. Pruski, Studies of organically functionalized mesoporous silicas using heteronuclear solid-state correlation NMR spectroscopy under fast magic angle spinning, J. Am. Chem. Soc. 127 (2005) 7587–7593.
[75] P. Sozzani, S. Bracco, A. Comotti, R. Simonutti, I. Camurati, Stoichlometric compounds of magnesium dichloride with ethanol for the supported Ziegler-Natta catalysis: first recognition and multidimensional MAS NMR study, J. Am. Chem. Soc. 125 (2003) 12881–12893.
[76] V. Ladizhansky, G. Hodes, S. Vega, Solid state NMR study of water binding on the surface of CdS nanoparticles, J. Phys. Chem. B 104 (2000) 1939–1943.
[77] J.M. Griffin, D.R. Martin, S.P. Brown, Distinguishing anhydrous and hydrous forms of an active pharmaceutical ingredient in a tablet formulation using solid-state NMR spectroscopy, Angew. Chem. Int. Ed. 46 (2007) 8036–8038.
[78] P. Charmont, A. Lesage, S. Steuernagel, F. Engelke, L. Emsley, Sample restriction using magnetic field gradients in high-resolution solid-state NMR, J. Magn. Reson. 145 (2000) 334–339.
[79] U. Haeberlen, High Resolution NMR Solids (1976).
[80] M. Mehring, J.S. Waugh, Magic-angle Nmr experiments in solids, Phys. Rev. B 5 (1972) 3459.
[81] B.J. van Rossum, G.J. Boender, F.M. Mulder, J. Raap, T.S. Balaban, A. Holzwarth, K. Schaffner, S. Prytulla, H. Oschkinat, H.J.M. de Groot, Multidimensional CP-MAS C-13 NMR of uniformly enriched chlorophyll, Spectrochim. Acta A Mol. Biomol. Spectrosc. 54 (1998) 1167–1176.
[82] M. Ernst, A. Verhoeven, B.H. Meier, High-speed magic-angle spinning C-13 MAS NMR spectra of adamantane: self-decoupling of the heteronuclear scalar interaction and proton spin diffusion, J. Magn. Reson. 130 (1998) 176–185.
[83] B.A.G. Xwin, NMR Software Manual, 1999.
[84] V.E. Zorin, M. Ernst, S.P. Brown, P. Hodgkinson, Insihts into homonuclear decoupling from effiient numerical simulation: techniques and examples, J. Magn. Reson. 192 (2008) 183–196.
[85] E. Vinogradov, P.K. Madhu, S. Vega, Strategies for high-resolution proton spectroscopy in solid-state NMR, New Techn. Solid-State NMR 246 (2005) 33–90.
[86] P.K. Madhu, E. Vinogradov, S. Vega, Multiple-pulse and magic-angle spinning aided double-quantum proton solid-state NMR spectroscopy, Chem. Phys. Lett. 394 (2004) 423–428.